

This is an Open Access document downloaded from ORCA, Cardiff University's institutional repository: <https://orca.cardiff.ac.uk/id/eprint/130400/>

This is the author's version of a work that was submitted to / accepted for publication.

Citation for final published version:

Li, Shuang, Li, Wei, Alves, Tiago M. , Wang, Jiliang, Feng, Yingci, Sun, Jie, Li, Jian and Wu, Shiguo 2020. Large-scale scours formed by supercritical turbidity currents along the full length of a submarine canyon, northeast South China Sea. *Marine Geology* 424 , 106158. 10.1016/j.margeo.2020.106158

Publishers page: <http://dx.doi.org/10.1016/j.margeo.2020.106158>

Please note:

Changes made as a result of publishing processes such as copy-editing, formatting and page numbers may not be reflected in this version. For the definitive version of this publication, please refer to the published source. You are advised to consult the publisher's version if you wish to cite this paper.

This version is being made available in accordance with publisher policies. See <http://orca.cf.ac.uk/policies.html> for usage policies. Copyright and moral rights for publications made available in ORCA are retained by the copyright holders.



# Large-scale scours formed by supercritical turbidity currents along the full length of a submarine canyon, northeast South China Sea

Shuang Li <sup>a, b, c</sup>, Wei Li <sup>a, b, c\*</sup>, Tiago M. Alves <sup>d</sup>, Jie Sun <sup>a, b, c</sup>, Yingci Feng <sup>a, b, c</sup>, Jian Li <sup>a, b, c</sup>, Shiguo Wu <sup>e</sup>

<sup>a</sup> CAS Key Laboratory of Ocean and Marginal Sea Geology, South China Sea Institute of Oceanology, Chinese Academy of Sciences, Guangzhou 510301, PR China

<sup>b</sup> University of Chinese Academy of Sciences, Beijing 100049, PR China

<sup>c</sup> Innovation Academy of South China Sea Ecology and Environmental Engineering, Chinese Academy of Sciences, Guangzhou 510301, China

<sup>d</sup> 3D Seismic Lab, School of Earth and Ocean Sciences, Cardiff University, Main Building, Park Place, Cardiff, CF10 3AT, United Kingdom

<sup>e</sup> Institute of Deep-sea Science and Engineering, Chinese Academy of Sciences, Sanya 572000, China

Correspondence to Dr. Wei Li (Email: [wli@scsio.ac.cn](mailto:wli@scsio.ac.cn))

## Abstract

High-resolution multi-beam bathymetric and seismic data enables a detailed morphological investigation of a submarine canyon (West Penghu Canyon) on the northeastern South China Sea margin, where twenty-three (23) scours are observed along the canyon thalweg. These scours form narrow topographic depressions in plan view and show asymmetrical morphologies in cross-section. The identified scours can be further divided into two groups (Type A and B scours) based on their sizes and relative locations. They are separated by a slope break at a water depth of ~2850 m. Type A scours (S1-S18) occur upslope from the slope break, whereas Type B scours (S19-S23) lie downslope from this same break. The scours are interpreted as net-erosional cyclic steps associated with turbidity currents flowing through the West Penghu Canyon; the currents that form Type A scours reveal higher

V, Q, and  $\Delta_{el}$  compared to Type B scours. A change in slope gradient and loss of lateral confinement are proposed to control the change from Type A to Type B scours. Furthermore, Coriolis force influences the flow direction of turbidity currents, leading to the preferential development and larger incisional depths of scours towards the southwestern flank of the West Penghu Canyon. Our results contribute to a better understanding on the origin of scours in submarine canyons across the world.

30

**Keywords:** South China Sea; Scours; Cyclic steps; Submarine canyon; Geomorphology; Coriolis force.

## 1 Introduction

Deep-water sedimentary processes, including gravity-driven downslope and along-slope processes, play a vital role in the shaping of continental margins (Rebesco et al., 2014; Mosher et al., 2017). Gravity-driven downslope sedimentary processes include a range of physical processes ranging from slides, slumps, and cohesive debris flows, which are able to form turbidity currents (Talling et al., 2012). Turbidity currents are themselves one of the most important processes transporting large volume (hundreds of km<sup>3</sup>) of sediment downslope from the continental slope into deep-marine environments (Paull et al., 2002; Talling et al., 2007). The morphology of continental margins can be modified by turbidity currents, leading to the generation of submarine canyons, channels, sediment waves and scours (Cartigny et al., 2014; Covault et al., 2014). Turbidity currents and related seafloor morphological features have been proposed to be fundamentally significant to channel initiation (Mchargue et al., 1991; Covault et al., 2014; Covault et al., 2017).

Cyclic steps are long-wave, upstream-migrating, upper-flow-regime bedforms bounded by

46 internal hydraulic jumps in turbidity currents (Covault et al., 2017). They are generally divided into  
47 two categories: net-depositional and net-erosional cyclic steps (Fildani et al., 2006; Lamb et al., 2008;  
48 Kostic, 2011; Covault et al., 2014; Postma and Cartigny, 2014; Zhong et al., 2015; Li and Gong,  
49 2018). Net-depositional cyclic steps take the form of upstream-migrating sediment waves relative to  
50 submarine channels (Fildani et al., 2006; Kostic et al., 2010; Cartigny et al., 2011; Kostic, 2011),  
51 while net-erosional cyclic steps are developed as trains of upstream-migrating scours (Kostic, 2011;  
52 Maier et al., 2011; Symons et al., 2016). Net-erosional cyclic steps (scours) are crescent-shaped to  
53 enclosed depressions that cut into the sea floor and have been identified in many a submarine canyon  
54 and channel, e.g. the Setúbal Canyon in West Iberia (Wynn et al., 2002), the Monterey East System  
55 in California (Fildani et al., 2006) and the Lucia Chica channel off central California (Maier et al.,  
56 2013). Net-erosional cyclic steps (scours) show closed topographic depressions, disrupted and  
57 discontinuous internal architecture, and less asymmetrical cross-sectional morphologies, stronger up-  
58 current migration than net-depositional cyclic steps (sediment waves).

59 The flow properties of turbidity currents generating the scours have been investigated by  
60 numerical stimulations (e.g. Fildani et al., 2006; Spinewine et al., 2009; Kostic, 2011) and physical  
61 experiments (e.g. Cartigny et al., 2014; Vellinga et al., 2017). Moreover, Li and Gong (2018) have  
62 quantitatively analyzed the difference between net-erosional cyclic steps (scours) and net-  
63 depositional cyclic steps (sediment waves). Turbidity currents flowing through net-erosional cyclic  
64 steps (scours) exhibit relatively higher flow velocity, bankfull discharge, and energy loss of hydraulic  
65 jump than net-depositional cyclic steps (sediment waves).

66 In contrast to the previous literature, this work focus on net-erosional cyclic steps developed  
67 along the full length of a submarine canyon, the West Penghu Canyon of the South China Sea (Figs.1

68 and 2). Here, a submarine canyon system, including nine N-S oriented submarine canyons, have been  
69 previously documented within the Taixinan Basin (Yin et al., 2015) (Fig. 2). High-frequency  
70 occurrences of turbidity currents have been reported in this region and related to high sediment supply  
71 (Murray et al., 2004; Ding et al., 2013), frequent earthquakes (Liu et al., 1999; Hsu et al., 2008; Gavey  
72 et al., 2016) and seasonal typhoons (Zhang et al., 2018). The study area is located in the northeastern  
73 part of the Taixinan Basin (Fig. 1), where the water depth ranges from 200 to 3400 m (Fig. 2). Zhong  
74 et al. (2015) have reported and investigated similar scours along the Taiwan Canyon and the West  
75 Penghu Canyon, and these scours were interpreted as cyclic steps. In this study, we find that the scours  
76 are distributed along the full length of the West Penghu Canyon, and its upper and middle reaches  
77 show much smaller scours than the lower reach. Scours on the lower reach also developed more  
78 closely to the southwest flank of the canyon (Figs. 3 to 6). As the flow properties of turbidity currents  
79 generating the scours in the West Penghu Canyon are still poorly understood, we undertook a  
80 quantitative analysis of these features using high-resolution multibeam bathymetric and multichannel  
81 seismic data, so that:

82 (a) The morphology and geometrical parameters of seafloor scours along a large submarine  
83 canyon could be investigated;

84 (b) The flow properties of turbidity currents crossing the scours could be determined;

85 (c) The factors controlling morphology changes of different types of scours were confirmed;

86 (d) The ways the Coriolis force affects the scours' distribution and development could be  
87 discussed in this work.

## 88    **2 Geological setting**

89        The South China Sea (SCS) is one of the largest marginal seas in the Pacific Ocean. It was first  
90    generated from Eocene to Middle Miocene (33-15.5 Ma) due to continental rifting from and  
91    subsequent seafloor spreading (Wang and Li, 2009; Li et al., 2014). Arc-continent collision between  
92    the Luzon Arc and the northern South China Sea margin around Taiwan, between the latest late  
93    Miocene and the early Pliocene, relates to an important regional tectonic event (Bowin et al., 1978;  
94    Suppe, 1981; Sibuet and Hsu, 1997). At the time, the eastern part of SCS was subducted under the  
95    Luzon Arc, generating the N-S oriented Manila Trench (Taylor and Hayes, 1983; Pautot et al., 1986).  
96    To the west, the SCS became bounded by a strike-slip fault zone offshore Vietnam (Taylor and Hayes,  
97    1983). As a result of this tectonic evolution, several sedimentary basins occur at present in the  
98    northern continental margin of South China Sea. From east to west, they are the Taixinan, Pearl River  
99    Mouth, Qiongdongnan and Yinggehai Basins (Xie et al., 2006).

100        The Taixinan Basin is bounded by the Dongsha Islands to the west and the Taiwan Island to the  
101    east (Fig. 1). It extends across the northern South China Sea and the south-western Taiwan continental  
102    slope (Fig. 1). Four major structural features, including the Northern Depression, the Central High,  
103    the Southern Depression, and the Southern High, are identified within the basin (Du, 1994; Lin et al.,  
104    2008). The basement of the basin is composed of Cretaceous sandstones, siltstones and shales  
105    deposited prior to the Cenozoic. In the Cenozoic, the basin was filled with Oligocene–Miocene shelf  
106    sandstones and mudstones, Pliocene shelf to deep-sea sandstones and mudstones, and Pleistocene  
107    deep-sea muds intercalated with sands and silts (Lee et al., 1993; Yu and Chen et al., 1994).

108        In the study area, a submarine canyon system consisting of nine (9) parallel submarine canyons  
109    comprise the most obvious bathymetric features on the northeast South China Sea (Zhong et al., 2015).

110 The West Penghu Canyon is located in the northwestern part of the Taixinan Basin (Fig. 2), with the  
111 Penghu High to the north and the Manila Trench to the south.

### 112 **3 Data and methods**

113 High-quality multibeam bathymetric and multichannel seismic data imaging the West Penghu  
114 Canyon in its whole length are used as the primary dataset in this work. The multibeam bathymetric  
115 data was imported and analyzed in the Global Mapper<sup>®</sup> software. A two-dimensional (2D)  
116 multichannel seismic profile was recently acquired by the South China Sea Institute of Oceanology,  
117 Chinese Academy of Sciences on May, 2019 using an 1800 m-long streamer with 144 channels. This  
118 acquisition geometry produced seismic traces with a spacing of 12.5 m. The frequency bandwidth of  
119 the seismic data is 30–45 Hz, providing an average vertical resolution of 11-17 m for the shallow  
120 strata. The data were processed using RadExpro<sup>®</sup> and interpreted using Geoframe<sup>®</sup>.

121 In this study, the bankfull flow properties of turbidity currents flowing along the West Penghu  
122 Canyon were calculated based on the morphological parameters of the interpreted canyon and  
123 associated scours. These morphological parameters include the wavelength, wave height, length and  
124 slope gradient of lee/stoss side of scours, and the bankfull depth and width of the West Penghu Canyon  
125 (Fig. 7b). These morphological parameters were used in several equations to calculate the flow  
126 properties of turbidity currents flowing through each scour, including the velocity ( $V$ ), discharge ( $Q$ ),  
127 Froude number ( $F_r$ ) and loss energy in the hydraulic jumps ( $\Delta_{el}$ ). Three parts are considered when the  
128 turbidity currents flow through a single scour: (1) at the base of the lee side just before the hydraulic  
129 jump, (2) at the crest of the scour, and (3) at the base of the stoss side just after the hydraulic jump  
130 (Fig. 7b). Parts (1) and (3) can be computed by Equations (1) to (7) derived from Konsoer (2013),

131 while part (2) of our computation derives from Equations (8) to (10) from Chanson et al (2004) (See  
132 supplementary material). The volume sediment concentration ( $C$ ) ranges from 0.2% to 0.6%, and the  
133 coefficient of friction at the bedforms ( $f$ ) is between 0.002 and 0.005 (Konsoer et al., 2013). We use  
134 a volume sediment concentration of 0.2%, and a friction coefficient of 0.005, as the best fits for both  
135 river and submarine environments (Konsoer et al., 2013). Other important parameters were gathered  
136 from Konsoer et al (2013) such as the gravitational acceleration ( $g=9.81 \text{ m}^2/\text{s}$ ), the Richardson  
137 number ( $R=1.65$ ), and the slope of the canyon ( $S=0.017$ ).

## 138 **4. Results**

### 139 **4.1 Scours along the West Penghu Canyon**

140 The West Penghu Canyon is located in the northeastern part of the interpreted bathymetric map  
141 and has a NW-SE orientation. It is 90-km long and occurs at a depth between 400 m to 2950 m in  
142 depth (Fig. 2). The width of the West Penghu Canyon varies from 5 to 10 km. A total of 23 scours  
143 have been identified along the West Penghu Canyon, comprising fully enclosed depressions with  
144 crescent-shaped crests at a water depth ranging from 2145 m to 2950 m (Figs. 5b and 6b). Most of  
145 the scours develop close to the southwestern flank of the West Penghu Canyon (Fig. 3a). A slope  
146 break can be distinguished at a water depth from 2845 m to 2865 m, showing an average slope  
147 gradient of  $0.02^\circ$  (Figs. 3a, b and c). Based on their location and sizes, the scours along the West  
148 Penghu Canyon can be classified in two types: a) scours developed in the upper reach of the slope  
149 break (Type A), and b) those located in the lower reach of the slope break, herein named Type B  
150 scours (Figs. 3a and b). The slope gradients of the stoss sides of the scours ( $\alpha$ ) range from  $1.11^\circ$  to  
151  $6.41^\circ$ , with a mean value of  $2.69^\circ$ , while the slope gradient of their lee sides ( $\beta$ ) range from  $0.42^\circ$  to



152 2.64°, or 1.23° on average (Fig. 8c). Scour asymmetry ( $A_y$ ) returns values of 0.18 to 2.02, with a mean  
153 value of 0.78 (Fig. 8b). W/H (wave length/ wave height) ratios increase when changing from Type A  
154 to Type B scours (Table 1; Fig. 8a).

#### 155 4.1.1 Type A scours

156 Type A scours occur in the upper and middle reaches of the West Penghu Canyon, at water depths  
157 from 2145 m to 2845 m, with an average slope gradient of 1.25°. Type A scours show a wavelength  
158 of 1.3-3.3 km and are 17-146 m high (Table 1). The length of the stoss side of Type A scours ( $L_{stoss}$ )  
159 ranges from 370 m to 1172 m, with a mean value of 771 m. The length of the lee side of Type A  
160 scours ( $L_{lee}$ ) ranges from 459 m to 2306 m, for an average of 1409 m (Table 1). The slope gradient of  
161 the stoss side of Type A scours ( $\alpha$ ) ranges from 1.11° to 6.41° for a mean value of 2.69°, while the  
162 slope gradient of their lee side ( $\beta$ ) ranges from 0.42° to 2.64°, with a mean value of 1.23° (Fig. 8c).  
163 The values of asymmetry ( $A_y$ ) of Type A scours range from 0.18 to 1.29, with 0.74 on average (Table  
164 1; Fig. 8b). Seismic profiles show that Type A scours S5 to S9 have obvious truncations reflections  
165 in both their stoss and lee sides (Figs. 4a and b).

166 Two trains of scours (S4-S14) can be distinguished in the upper reach of the West Penghu Canyon  
167 (Fig. 5). They are separated by a positive bathymetric feature (an intra-canyon high) at water depths  
168 between 2272 m and 2612 m (Fig. 5a). On the bathymetric profiles, the scours to the southwest have  
169 larger incision depths than their counterparts to the northeast. The differences in depth between parts  
170 of these scours are 25 m, 30 m and 16 m, respectively (Table 3).

#### 171 4.1.2 Type B scours

172 Type B scours are located in the lower reach of the West Penghu Canyon at a water depth from

173 2865 m to 2950 m, in a region with an average slope gradient of  $0.38^\circ$ . Type B scours have  
174 wavelengths of 1.5-4.7 km and are 30-93 m high (Table 1). The length of the stoss side of Type B  
175 scours ( $L_{\text{stoss}}$ ) ranges from 876 m to 2381 m, with a mean value of 1718 m. The length of the lee side  
176 of Type B scours ( $L_{\text{lee}}$ ) is 603 m to 2349 m, for an average of 1374 m (Table 1). The slope gradient  
177 of the stoss side of Type B scours ( $\alpha$ ) ranges from  $1.02^\circ$  to  $3.16^\circ$ , with a mean value of  $2.09^\circ$ , while  
178 the slope gradient of the lee side ( $\beta$ ) ranges from  $0.9^\circ$  to  $1.53^\circ$ , with a mean value of  $1.22^\circ$  (Fig. 8c).  
179 The values of asymmetry ( $A_y$ ) of Type B scours range from 0.78 to 2.03, with an average of 1.41  
180 (Table 1; Fig. 8b). On seismic profiles, Type B scours S19 to S23 show trains of upstream-migrating  
181 scours (Fig. 4a). Cross-section profiles show sub-parallel or parallel reflections draping each of the  
182 five scours (Figs. 4a and c). Truncated reflections can be observed in their lee sides and minor  
183 upstream accretion occurs in their stoss sides (Figs. 4a and c).

#### 184 **4.2 Flow properties of turbidity currents generating the scours**

185 Flow properties of turbidity currents along the West Penghu Canyon are calculated using  
186 Equations (1) to (7) based on the scours' morphological characters. The flow velocity of turbidity  
187 currents before hydraulic jumps occur ( $V_1$ ) ranges from 5.4 m/s to 11.8 m/s (8.8 m/s on average)  
188 (Table 2; Fig. 9a). The flow discharge of turbidity currents before the hydraulic jumps ( $Q_1$ ) ranges  
189 from  $7.2 \times 10^5 \text{ m}^3/\text{s}$  to  $3.8 \times 10^7 \text{ m}^3/\text{s}$  (Table 2; Fig. 9b), and  $Fr_1$  is a stable value (2.13) with a small  
190 change (Table 2; Fig. 9c).

191 The  $V_1$  and  $H_1$  of turbidity currents were used in Equations (8) to (10) to compute  $V_2$  (flow  
192 velocity after hydraulic jumps),  $H_2$  (flow depth post hydraulic jumps) and  $Fr_2$  (Froude number of  
193 turbidity currents during hydraulic jumps). The velocity of the turbidity currents after the hydraulic

194 jumps ( $V_2$ ) ranges from 2.8 m/s to 8.8 m/s, with a mean value of 6.6 m/s, and  $Fr_2$  is a stable value  
195 ranging between 0.5 and 0.6 (Table 2; Figs. 9a, b and c). The loss of energy recorded by the turbidity  
196 currents during the hydraulic jumps ( $\Delta_{el}$ ) can be calculated by equation 11. It ranges from 0.6 m and  
197 6.2 m with a mean value of 3.6 m (Table 2; Fig. 9d). The flow properties of turbidity currents on the  
198 crest of these scours ( $V_3$ ,  $Q_3$ ,  $Fr_3$ ) can also be calculated by Equations (1) to (7). Here,  $V_3$  ranges from  
199 2.4 m/s and 11.6 m/s (averaging 7.9 m/s),  $Q_3$  ranges from  $5.1 \times 10^5 \text{ m}^3/\text{s}$  and  $3.5 \times 10^7 \text{ m}^3/\text{s}$  (averaging  
200  $1.7 \times 10^7 \text{ m}^3/\text{s}$ ) and  $Fr_3$  is 2.13 (Table 2; Figs. 9a, b and c).

201 Before the hydraulic jumps, the velocity of turbidity currents flowing through Type A scours ( $V_1$ )  
202 ranges from 7.8 m/s to 11.8 m/s (averaging 9.8 m/s) (Table 2; Fig. 9a). The flow discharge of turbidity  
203 currents flowing through Type A scours ( $Q_1$ ) ranges from  $1.1 \times 10^7 \text{ m}^3/\text{s}$  to  $3.8 \times 10^7 \text{ m}^3/\text{s}$  (Table 2; Fig.  
204 9b). Importantly, there is a significant decrease in the velocity ( $V$ ) and discharge ( $Q$ ) of turbidity  
205 currents when comparing Type A with Type B scours. The velocity of turbidity currents flowing  
206 through Type B scours ( $V_1$ ) ranges from 3.8 m/s to 5.8 m/s (4.8 m/s on average) (Table 2; Fig. 9a).  
207 The flow discharge of turbidity currents flowing through Type B scours ( $Q_1$ ) ranges from  $7.3 \times 10^5$   
208  $\text{m}^3/\text{s}$  to  $3.9 \times 10^6 \text{ m}^3/\text{s}$  (Table 2; Fig. 9b). Immediately after the hydraulic jumps, the velocity of turbidity  
209 currents flowing through Type B scours ( $V_2$ ) ranges from 5.8 m/s to 8.8 m/s (averaging 7.3 m/s)  
210 (Table 2; Fig. 9a).

211 The loss of energy in turbidity currents during hydraulic jumps ( $\Delta_{el}$ ) can be calculated by  
212 Equation 11, and range from 2.7 m and 6.2 m with a mean value of 4.5 m (Table 2; Fig. 9d). An  
213 obvious decrease in the velocity of turbidity currents after the hydraulic jumps, and a loss energy of  
214 turbidity currents during these same jumps, can be observed at the limit between Type A and Type B  
215 scours. Here, the velocity of turbidity currents flowing through Type B scours ( $V_2$ ) ranges from 2.8

216 m/s to 4.3 m/s (3.6 m/s in average) (Table 2; Fig. 9a). The loss of energy in turbidity currents during  
217 hydraulic jumps ( $\Delta e_l$ ) of Type B scours ranges from 0.6 m and 1.5 m with a mean value of 1.1 m  
218 (Table 2; Fig. 9d). In the third stage, the values of flow properties of turbidity currents on the crests  
219 of Type A scours ( $V_3$ ,  $Q_3$ ) range from 7.4 m/s to 11.6 m/s (9.5 m/s in average) and from  $1 \times 10^7 \text{ m}^3/\text{s}$   
220 to  $3.5 \times 10^7 \text{ m}^3/\text{s}$  ( $2.8 \times 10^7 \text{ m}^3/\text{s}$  in average), respectively.

221 In the transition from Type A to B scours, the flow conditions of turbidity currents also show an  
222 obvious decrease. The velocity of turbidity currents on the crests of Type B scours ( $V_3$ ) ranges from  
223 2.4 m/s to 3.4 m/s (2.9 m/s in average). The flow discharge of turbidity currents on the crests of Type  
224 B scours ( $Q_3$ ) ranges from  $5.1 \times 10^5 \text{ m}^3/\text{s}$  to  $8.2 \times 10^6 \text{ m}^3/\text{s}$ , averaging  $4.4 \times 10^6 \text{ m}^3/\text{s}$  (Table 2; Figs. 9a, b  
225 and c).

#### 226 **4.3 Differences in morphological and hydraulic properties between Type A and B scours**

227 The wavelengths of Type A scours are 1-1.5 times larger than Type B scours, while the  
228 waveheights of the Type A scours are 0.2-0.6 times smaller than Type B scours (Table 1). The length  
229 of the stoss side of Type B scours ( $L_{\text{stoss}}$ ) is 2.3-6.4 times longer than Type A scours, while the length  
230 of the lee side ( $L_{\text{lee}}$ ) and the full length of Type B scours are 1-5.4 times and 1.4-3.5 times, respectively  
231 (Table 1). The slope gradient of the stoss side of Type A scours ( $\alpha$ ) is 1-2 times larger than Type B  
232 scours, while the slope gradient of the lee side ( $\beta$ ) of Type A scours is 1.7-2.9 times larger than Type  
233 B scours. The values of asymmetry ( $A_y$ ) of Type B scours are 1.6-4.3 times larger than Type A scours  
234 (Table 1). In terms of their hydraulic characteristics, values of  $V_1$ ,  $Q_1$ , and  $\Delta e_l$  for turbidity currents  
235 forming Type A scours (S1 to S18) are 1-3 times, 13-50 times, and 4-6 times larger than those forming  
236 Type B scours (S19 to S23), respectively.

## 237 5. Discussion

### 238 5.1 Origin of the scours along the West Penghu Canyon

239 In this study, 23 scours have been identified along the West Penghu Canyon; they all form fully  
240 enclosed depressions with crescent-shaped crests (Figs. 3a, b and c). Symons et al. (2016) have  
241 conducted a statistical analysis on a number of scours spanning a broad range of water depths and  
242 environments. In the study area, the wavelengths and wave heights of the scours are comparable to  
243 the large-scale scours documented in Symons et al. (2016) (see Fig. 10). We find that these scours  
244 comprise large-scale erosional bedforms, but their origin is still not clear.

245 Scours within submarine canyons have been related to supercritical turbidity currents and  
246 associated hydraulic jumps (Fidani et al., 2006; Symons et al., 2016; Hage et al., 2018). Numerical  
247 and physical modelling has confirmed that hydraulic jumps occur along the flow paths of turbidity  
248 currents captured by submarine canyons (Fildani et al., 2006; Kostic and Parker, 2006; Postma et al.,  
249 2009; Kostic, 2011; Cartigny et al., 2011;). The formation of scours is determined by the occurrence  
250 of hydraulic jumps, where a flow makes a rapid transition from a thin, rapid supercritical flow (Froude  
251 number  $> 1$ ) to a thick, slow subcritical flow (Froude number  $< 1$ ) (Fildani et al., 2006; Normark et  
252 al., 2009). In this study, 23 scours along the West Penghu Canyon show continuous changes in Froude  
253 number (Fig. 9), indicating that the scours are linked to the formation of hydraulic jumps. Therefore,  
254 the formation of the large-scale scours along the West Penghu Canyon can be attributed to the  
255 transition from supercritical to subcritical turbidity currents.

256 After the concept of supercritical and subcritical flows was introduced (Kostic and Parker et al.,  
257 2006; Fildani et al., 2006; Lamb et al., 2008), most scours in submarine canyons and channels were

identified as net-erosional cyclic steps (e.g., Kostic, 2011). For instance, Zhong et al. (2015) grouped the scours along the West Penghu Canyon into two main categories. They considered our Type A scours (S1 to S18) as net-erosional cyclic steps, while Type B scours (S19-S23), identified downslope from the slope break, were net-depositional cyclic steps according to Zhong et al. (2015). This work shows these scours to be enclosed depressions on the contour maps (Figs. 5c and 6c), forming trains of asymmetrical waveforms in a characteristic upslope migration in cross-section (Figs. 3c and 4c). The multichannel seismic profiles in this work also show truncations in some scours (S5-S7; S19-S23), suggesting erosion of seafloor sediment (Figs. 4a, b and c). This latter character indicates that scours are all bounded by hydraulic jumps of overriding, alternating Froude-supercritical to subcritical turbidity currents; loss of strata is attributed to erosion by turbidity currents (Covault et al., 2014). The scours identified in this study are similar to those documented along the Monterey East Channel, which are interpreted as net-erosional cyclic steps (Fildani et al., 2006; Symons et al., 2016). Thus, we think Type A and B scours should be interpreted as net-erosional cyclic steps.

## **5.2 Factors controlling the shift from Type A to Type B scours**

The large-scale scours in the study area could be divided into two main types (Type A and B) based on their locations and sizes (Figs. 3a and b). Type A scours are observed in the upper reach of the West Penghu Canyon (Fig. 5), while Type B scours develop in the lower reach (Fig. 5). In plan view, Type A scours are much smaller compared to Type B scours (Figs. 3a, 3b and 4a). On the cross-section profile, Type A scours have an average slope gradient of  $1.25^\circ$ , while Type B scours have a slope gradient of only  $0.38^\circ$  on average (Fig. 3c). In detail, the flow properties of turbidity currents crossing Type A and B scours show a pronounced decrease in the flow velocity (11.8 m/s to 3.1m/s),

279 flow discharge (from  $3.8 \times 10^7 \text{ m}^3/\text{s}$  to  $5.1 \times 10^5 \text{ m}^3/\text{s}$ ) and loss of energy (from 6.17 to 0.63) (Fig. 9;  
280 Table 2). Such a dramatic change in the properties of turbidity currents has seldom been documented  
281 in submarine canyons and channels, and raises questions about the true physical factors controlling  
282 the transition from Type A to Type B scours.

283 Factors such as slope gradient, sediment concentration, bed roughness and entrainment  
284 coefficient, have been considered to play a vital role in changing the flow regimes of turbidity currents  
285 in submarine canyons (Kostic and Parker 2006; Kostic 2011). Variations of slope steepness can result  
286 in the changes in both the dominant erosion process and the controlling sediment regime along  
287 submarine canyons (Huang and Laflen, 1996; Gabbard et al., 1998; Huang, 1998). The presence of a  
288 slope break in the West Penghu Canyon may also lead to the decrease of flow velocity, discharge and  
289 energy loss of turbidity currents (Figs. 9a, c and d). As a consequence of such a slope break, the  
290 erosional capacity of turbidity currents may be reduced, explaining why Type A scours have smaller  
291 wavelengths and larger wave heights than Type B scours (Fig. 8). Therefore, we propose that the  
292 change of slope gradient (due to the presence of the slope break) has a marked effect on the change  
293 from Type A to Type B scours along the West Penghu Canyon.

294 The relationship between morphologies of scours ( $L_{\text{stoss}}$  and  $A_y$ ) and properties of turbidity  
295 currents ( $V_1$ ,  $Q_1$  and  $\Delta_{\text{el}}$ ) are shown in Figure 11. The power law relationships amongst  $L_{\text{stoss}}$  and  $V_1$ ,  
296  $Q_1$ , and  $\Delta_{\text{el}}$  show average correlation coefficient ( $R^2$ ) values of 0.356 to 0.401 (Figs. 11a, 11d and 11g).  
297 The relationship amongst  $A_y$  and  $V_1$ ,  $Q_1$  and  $\Delta_{\text{el}}$  also reveals an average correlation coefficient, with  
298 Type A scours showing less asymmetry than Type B scours (Figs. 11b, 11d and 11h). Plots of  $W_1/H_1$   
299 against  $V_1$ ,  $Q_1$  and  $\Delta_{\text{el}}$  show clear power law relationships with  $R^2$  values close of above 0.9 (Figs.  
300 11c, 11f and 11i). The dramatic change in  $V_1$ ,  $Q_1$  and  $\Delta_{\text{el}}$  of turbidity currents downstream suggests a

301 decrease in the sediment-transport capacity of turbidity currents, a change associated in this work to  
302 the presence of the slope break previously mentioned. This downstream decrease in  $V_1$ ,  $Q_1$  and  $\Delta_{el}$   
303 probably drives the progressive change in morphological characteristics of scours, including the  
304 observed increase in  $L_{stoss}$ ,  $A_y$  and  $W_1/H_1$  downstream (Li and Gong et al., 2018).

305 Recent physical experiments have shown that abrupt losses in the lateral confinement of canyons  
306 can lead to flow relaxation and a decrease in flow velocity (de Leeuw et al., 2016; Pohl et al., 2019).  
307 Moreover, spatial and temporal variations in flow velocity affect the ability of turbidity flows to  
308 transport sediment (de Leeuw et al., 2016). In our case, Type A scours (S1-S18) develop within a  
309 narrow area (~3.6 km in width) in the West Penghu Canyon, and Type B scours (S19-S23) are  
310 distributed in a wider area (~5.5 km in width) (Figs. 3, 5, 6). The levee height of the canyon flanks  
311 ranges from 182 m to 463 m in the upper canyon reach where the Type A scours occur. Conversely,  
312 it ranges from 19 m to 110 m in the lower canyon reach where the Type B scours are observed (Table  
313 1). We postulate that the increase in canyon width and the decrease in the height of canyon flanks led  
314 to the loss of lateral support for turbidity currents. Lateral spreading and thinning thus occur in the  
315 lower reach of the West Penghu Canyon, correlating with a dramatic change in the flow regime of  
316 turbidity currents crossing from Type A to Type B scours (Figs. 9a, c and d). The erosional depths of  
317 Type B scours are smaller compared to Type A, a character that can be correlated with a decrease in  
318 the velocity of turbidity currents.

319 In summary, we propose that both the change of slope gradient and the loss of lateral confinement  
320 are main controls on the flow properties of turbidity currents, and have led to the change from Type  
321 A to Type B scours in the West Penghu Canyon.



### 322 5.3 The role of Coriolis force on the distribution and development of scours

323 The Coriolis force acts as a complementary centrifugal force in the world's oceans and seas,  
324 changing the direction of a moving body to the right in the Northern Hemisphere and to the left in the  
325 Southern Hemisphere (Persson et al., 1998; Persson et al., 2000). The effect of the Coriolis force upon  
326 turbidity currents has been identified in previous numerical simulations and physical experiments (e.g.  
327 Jones et al. 2006; Wells, 2009; Cossu et al., 2010). Wells (2009) proposed that if turbidity currents  
328 traverse a large distance in a time-scale comparable to one day, then the Coriolis force will result in  
329 a significant deflection of the turbidity currents to the right in the Northern hemisphere. If the turbidity  
330 currents flow towards the south, it would result in more erosion on the western margin of the canyons,  
331 and more deposition on the eastern counterpart (Cossu and wells, 2013). The importance of Coriolis  
332 forces affecting turbidity currents can be expressed with the Rossby number (Cossu and Well et al.,  
333 2013). Coriolis forces can play a key role in controlling the morphology of submarine canyons when  
334 Rossby numbers are small ( $R_0 < 10$ ) (Cossu et al., 2010).

335 The calculated Rossby numbers for the West Penghu Canyon range from 10 to 21.6, suggesting  
336 that the Coriolis force does not play a significant role on the flow direction of turbidity currents.  
337 However, two trains of scours (S4-S14) can be distinguished in the upper reach of the West Penghu  
338 Canyon (Figs. 5a, b and c). They are separated by a positive bathymetric feature (an intra-canyon  
339 high), which is located at a water depth of 2272 m to 2612 m (Figs. 5a and 13a). This intra-canyon  
340 high is ~10 km in length, 2 km in width and 30–120 m in height (Zhong et al., 2015; Figs. 12a, b and  
341 c). According to our interpretation, turbidity currents can be split into two branches when meeting the  
342 intra-canyon high, leading to the formation of two trains of scours in the upper reach of the West  
343 Penghu Canyon. Based on the bathymetric profiles in this work, the southwest train of scours has a

344 larger incised depth to the one to the northeast (Figs. 13a, b and c). In order to explain this  
345 phenomenon, one needs to consider that turbidity currents flowing through the West Penghu Canyon  
346 are deviated to the southwest due to the Coriolis force. This leads to more erosion and larger incised  
347 depths in the southwest side of the intra-canyon high.

348 The scours in the middle and lower reaches of the West Penghu Canyon are distributed close to  
349 the southwest canyon flank (Figs. 6a, b and c). Bathymetric isobaths adjacent to this flank are closer  
350 together than those on the northeast flank (Fig. 6c). This indicates that the southwest canyon flank is  
351 relatively (and frequently) more eroded by turbidity currents. When flowing through the middle and  
352 lower reaches of the canyon, turbidity currents are forced to the southwest and erode the southwest  
353 flank of the canyon. This explains why this latter flank is much steeper and more scours develop on  
354 it (Fig. 14).

## 355 **6 Conclusions**

356 High-resolution bathymetric and seismic data allow us to investigate the origin, transition and  
357 development of scours along the full length of the West Penghu Canyon, northeastern South China  
358 Sea. The main conclusions of this work are as follows:

359 (1) Twenty-three (23) scours have been identified along the thalweg of West Penghu canyon,  
360 northeast continental slope of South China Sea. These scours can be sub-divided into two types, Type  
361 A and Type B, based on their locations and sizes.

362 (2) These scours are revealed as closed topographic depressions in plan view and show  
363 asymmetrical morphologies in cross-section. The origin of these scours is related to the strength of  
364 turbidity currents flowing through the West Penghu Canyon. They are all interpreted as net-erosional

365 cyclic steps.

366 (3) Type A scours are more symmetric, show a wider range in slope angle ( $\alpha$ ,  $\beta$ ,  $\theta$ ), larger wave  
367 heights and smaller wavelengths, when compared to Type B scours. Turbidity currents flowing  
368 through Type A scours reflect higher  $V$  (flow velocity),  $Q$  (flow discharge), and  $\Delta_{el}$  (energy loss of  
369 hydraulic jump) than those crossing Type B scours.

370 (4) The main factors controlling the observed shift from Type A to B scours are the presence of  
371 slope break in the middle of the canyon (2845 m-2865 m) and the loss of lateral confinement of the  
372 canyon.

373 (5) The Coriolis force is revealed as a prominent influence on the deflection of turbidity currents  
374 to the southwest. Therefore, several Type A scours located in the west of the intra-canyon high show  
375 larger incision depths than those in the east. Moreover, more scours occur close to the southwest flank  
376 of the West Penghu canyon.

## 377 **Acknowledgements**

378 This work was financially supported by the National Scientific Foundation of China (Grant No.  
379 41876054). Dr. Wei Li is funded by the CAS Pioneer Hundred Talents Program. Dr. Matthieu  
380 Cartigny and Dr. Jacob Covault are thanked for their suggestions on an earlier version of this  
381 manuscript. This paper benefited from constructive comments by the Editor and reviewers.

## 382 **References**

383 Arzola, R.G., Wynn, R.B., Lastras, G., Masson, D.G., Weaver, P. P. E., 2008. Sedimentary features and processes in  
384 the Nazaré and Setúbal submarine canyons, west Iberian margin. *Marine Geology*. 250, 64-88.

385 Bowin, C., Lu, S.R., Lee, C.S., Schouten, H., 1978. Plate Convergence and Accretion in Taiwan-Luzon Region. AAPG  
386 Bulletin (American Association of Petroleum Geologists). 62, 1645-1672.

387 Cartigny, M.J.B., Ventra, D., Postma, G., van Den Berg, J.H., Venditti, J., 2014. Morphodynamics and sedimentary  
388 structures of bedforms under supercritical-flow conditions: New insights from flume experiments. *Sedimentology*.  
389 61, 712-748.

390 Cartigny, M.J.B., Postma, G., van den Berg, J.H., Mastbergen, D.R., 2011. A comparative study of sediment waves  
391 and cyclic steps based on geometries, internal structures and numerical modeling. *Marine Geology*. 280, 40-56.

392 Chanson, H., 2004. *Hydraulics of Open Channel Flow, An Introduction Basic Principles, Sediment Motion, Hydraulic*  
393 *Modelling. Design of Hydraulic Structure*, Butterworth-Heinemann, Oxford, UK. p. 53–63.

394 Cossu, R., Wells, M., Wahlin, A., 2010. Influence of the Coriolis force on the velocity structure of gravity currents in  
395 straight submarine channel systems. *Journal of Geophysical Research-Oceans*. 115.

396 Cossu, R., Wells, M., 2013. The evolution of submarine channels under the influence of Coriolis forces: experimental  
397 observations of flow structures. *Terra Nova*. 25, 65-71.

398 Covault, J.A., Kostic, S., Paull, C.K., Ryan, H.F., Fildani, A., Talling, P., 2014. Submarine channel initiation, filling  
399 and maintenance from sea-floor geomorphology and morphodynamic modelling of cyclic steps. *Sedimentology*.  
400 61, 1031-1054.

401 Covault, J.A., Kostic, S., Paull, C.K., Sylvester, Z., Fildani, A., 2017. Cyclic steps and related supercritical bedforms:  
402 Building blocks of deep-water depositional systems, western North America. *Marine Geology*. 393, 4-20.

403 de Leeuw, J., Eggenhuisen, J.T., Cartigny, M.J.B., 2016. Morphodynamics of submarine channel inception revealed  
404 by new experimental approach. *Nat Commun*. 7, 10886.

405 Ding, W., Franke, D., Li, J., Steuer, S., 2013. Seismic stratigraphy and tectonic structure from a composite multi-  
406 channel seismic profile across the entire Dangerous Grounds, South China Sea. *Tectonophysics*. 582, 162-176.

407 Fildani, A., Normark, W.R. Kostic, S., Parker, G., 2006. Channel formation by flow stripping: large-scale scour  
 408 features along the Monterey East Channel and their relation to sediment waves. *Sedimentology*. 53, 1265-1287.

409 Feng, D., Cheng, M., Kiel, S., Qiu, J.W., Yang, Q., Zhou, H., Peng, Y., Chen, D., 2015. Using Bathymodiolus tissue  
 410 stable carbon, nitrogen and sulfur isotopes to infer biogeochemical process at a cold seep in the South China Sea.  
 411 *Deep Sea Research Part I Oceanographic Research Papers*. 104, 52-59.

412 Gabbard, D.S., Huang, C., Norton, L.D., Steinhardt, G.C., 1998. Landscape position, surface hydraulic gradients and  
 413 erosion processes. *Earth Surface Processes and Landforms*. 23, 83–93.

414 Gavey, R., Carter, L., Liu, J., Talling, P.J., Hsu, R.T., Pope, E., Evans, G., 2016. Frequent sediment density flows  
 415 during 2006 to 2015, triggered by competing seismic and weather events: Observations from subsea cable breaks  
 416 off southern Taiwan. *Marine Geology - MAR GEOLOGY*. 384, 147-158.

417 Gong, C.L., Wang, Y., Zhu, W., Li, W.G., Xu, Q., Zhang, J.M., 2011. The Central Submarine Canyon in the  
 418 Qiongdongnan Basin, northwestern South China Sea: Architecture, sequence stratigraphy, and depositional  
 419 processes. *Marine & Petroleum Geology*. 28, 0-1702.

420 Hage, S., M. J. B. Cartigny., M. A. Clare., E. J. Sumner., D. Vendettuoli., J. E. Hughes Clarke., S. M. Hubbard., P. J.  
 421 Talling., D. G. Lintern., C. D. Stacey., R. G. Englert., M. E. Vardy., J. E. Hunt., M. Yokokawa., D. R. Parsons., J.  
 422 L. Hizzett., M. Azpiroz-ZabalaA. J. Vellinga., 2018. How to recognize crescentic bedforms formed by  
 423 supercritical turbidity currents in the geologic record: Insights from active submarine channels. *Geology*. 46: 563-  
 424 566.

425 Hsu, S.K., Kuo, J., Yeh, Y.C., Tsai, C.H., Doo, W., Ku, C.Y., Sibuet, J.C., 2008. Turbidity Currents, Submarine  
 426 Landslides and the 2006 Pingtung Earthquake off SW Taiwan. *AGU Fall Meeting Abstracts*. 19, 767.

427 Huang, C.H., Laflen, J.M., 1996. Seepage and Soil Erosion for a Clay Loam Soil. *Science Society of America Journal*.  
 428 60, 408-416.

429 Jones, O.P., Simons, R., Jones, E., Harris, J.M., 2006. Influence of seabed slope and Coriolis effects on the  
430 development of sandbanks near headlands. *Journal of Geophysical Research*. 111.

431 Komar, P.D., 1969. The channelized flow of turbidity currents with application to Monterey Deep-Sea Fan Channel.  
432 *Journal of Geophysical Research*. 74: 4544-4558.

433 Konsoer, K., Zinger, J., Parker, G., 2013. Bankfull hydraulic geometry of submarine channels created by turbidity  
434 currents: Relations between bankfull channel characteristics and formative flow discharge. *Journal of*  
435 *Geophysical Research: Earth Surface*. 118, 216-228.

436 Kostic, S., Parker, G., 2006. The response of turbidity currents to a canyon-fan transition: Internal hydraulic jumps  
437 and depositional signatures. *Journal of Hydraulic Research - J HYDRAUL RES*. 44, 631-653.

438 Kostic, S., Sequeiros, O., Spinewine, B., Parker, G., 2010. Cyclic steps: A phenomenon of supercritical shallow flow  
439 from the high mountains to the bottom of the ocean. *Journal of Hydro-environment Research*. 3, 167-172.

440 Kostic, S., 2011. Modeling of submarine cyclic steps: Controls on their formation, migration, and architecture.  
441 *Geosphere*. 7, 294-304.

442 Lamb, M.P., Parsons, J.D., Mullenbach, B.L., Finlayson, D.P., Orange, D.L., Nittrouer, C.A., 2008. Evidence for  
443 superelevation, channel incision, and formation of cyclic steps by turbidity currents in Eel Canyon, California.  
444 *Geological Society of America Bulletin*. 120, 463-475.

445 Lee, T.Y., Tang, C.H., Ting, J.S., Hsu, Y.Y., 1993. Sequence stratigraphy of the Tainan Basin, offshore southwestern  
446 Taiwan. *Petroleum Geology of Taiwan*. 28, 119-158.

447 Li, C.F., Xu, X., Lin, J., Sun, Z., Zhu, J., Yao, Y., Zhao, X., Liu, Q., Kulhanek, D., Wang, J., Song, T., Zhao, J., Qiu,  
448 N., Guan, Y., Zhou, Z., Williams, T., Bao, R., Briais, A., A. Brown, E., Zhang, G.L., 2014. Ages and magnetic  
449 structures of the South China Sea constrained by deep tow magnetic surveys and IODP Expedition 349.  
450 *Geochemistry, Geophysics, Geosystems*. 15.

451 Li, L., Gong, C.L., 2018. Gradual Transition From Net Erosional to Net Depositional Cyclic Steps Along the  
 452 Submarine Distributary Channel Thalweg in the Rio Muni Basin: A Joint 3-D Seismic and Numerical  
 453 Approach. *Journal of Geophysical Research: Earth Surface*. 123, 2087-2106.

454 Lin, A., Liu, C.S., Lin, C.C., Schnurle, P., Chen, G.Y., Liao, W.Z., S. Teng, L., Chuang, H.-J., Wu, M.-S., 2008.  
 455 Tectonic features associated with the overriding of an accretionary wedge on top of a rifted continental margin:  
 456 An example from Taiwan. *Marine Geology - MAR GEOLOGY*. 255, 186-203.

457 Liu, J., Chao, Y.S., Hsu, R.T., 1999. The influence of suspended sediments on the plume of a small mountainous river.  
 458 *Journal of Coastal Research*. 15, 1002-1010.

459 Maier, K.L., Fildani, A. Paull, C.K., Graham, S.A., McHargue, T.R., Caress, D.W., McGann, M., 2011. The elusive  
 460 character of discontinuous deep-water channels: New insights from Lucia Chica channel system, offshore  
 461 California. *Geology*. 39, 327-330.

462 Mchargue T R., 1991. Seismic Facies, Processes, and Evolution of Miocene Inner Fan Channels, Indus Submarine  
 463 Fan. *Seismic Facies and Sedimentary Processes of Submarine Fans and Turbidite Systems*. Springer New York.

464 Mosher, D. C., Campbell, D. C., Gardner, J. V., Piper, D. J. W., Chaytor. J. D., Rebesco. M., 2017. The role of deep-  
 465 water sedimentary processes in shaping a continental margin: The Northwest Atlantic. *Marine Geology*. 393: 245-  
 466 259.

467 Paull, C., Greene, H., Ussler, B., Mitts, P.J., 2002. Pesticides as tracers of sediment transport through Monterey Canyon.  
 468 *Geo-Marine Letters*. 22, 121-126.

469 Pautot, G., Rangin, C., Briais, A., Tapponnier, P., Beuzart, P., Lericolais, G., Mathieu, X., Wu, J., Han, S., Li, H., Lu,  
 470 Y., Zhao, J., 1986. Spreading direction in the central South China Sea. *Nature*. 321, 150-154.

471 Persson, A., 1998. How Do We Understand the Coriolis Force? *Bulletin of the American Meteorological Society*. 791,  
 472 373-1385.

473 Persson, A., 2000. Back to basics: Coriolis: Part 3 - The Coriolis force on the physical earth. *Weather*. 55, 234-239

474 Postma, G., Cartigny, M.J.B., Kleverlaan, K., 2009. Structureless, coarse-tail graded Bouma Ta formed by internal  
475 hydraulic jump of the turbidity current? *Sedimentary Geology*. 219, 1-6.

476 Postma, G., Kleverlaan, K., Cartigny, M.J.B., Mohrig, D., 2014. Recognition of cyclic steps in sandy and gravelly  
477 turbidite sequences, and consequences for the Bouma facies model. *Sedimentology*. 61, 2268-2290.

478 Normark, R., Paull, W.C., Caress, D., Ussler, B., Sliter, R.A.Y., 2009. Fine-scale relief related to Late Holocene  
479 channel shifting within the floor of the upper Redondo Fan, offshore Southern California. *Sedimentology*. 56,  
480 1690-1704.

481 Rebesco, M., Hernández-Molina, F., Van Rooij, D., Wählin, A., 2014. Contourites and associated sediments controlled  
482 by deep-water circulation processes: State-of-the-art and future Considerations. *Marine Geology - MAR*  
483 *GEOLOGY*. 352, 10-12

484 Sibuet, J.C., Hsu, S.K., 1997. Geodynamics of Taiwan arc–arc collision. *Tectonophysics* 274, 221-251.

485 Symons, W.O., Sumner, E.J., Talling, P.J., Cartigny, M.J.B., Clare, M.A., 2016. Large-scale sediment waves and  
486 scours on the modern seafloor and their implications for the prevalence of supercritical flows. *Marine Geology*.  
487 371, 130-148.

488 Spinewine, B., Sequeiros, O., García, M., Beaubouef, R., Sun, T., Savoye, B., Parker, G., 2009. Experiments on  
489 Wedge-Shaped Deep Sea Sedimentary Deposits in Minibasins and/or on Channel Levees Emplaced by Turbidity  
490 Currents. Part II. Morphodynamic Evolution of the Wedge and of the Associated Bedforms. *Journal of*  
491 *Sedimentary Research - J SEDIMENT RES.* 79, 608-628.

492 Suppe, J., 1981. Mechanics of mountain building and metamorphism in Taiwan. *Memoir of the Geological Society of*  
493 *China (Taiwan)*. 4, 67-89.

494 Talling, P.J., Wynn, R.B., Masson, D.G., Frenz, M., Cronin, B., Schiebel, R., Akhmetzhanov, A.M., Dallmeier-Tiessen,



495 S., Benetti, S., Weaver, P., Georgiopolou, A., Zühlendorff, C., Amy, L., 2007. Onset of submarine debris flow  
 496 deposition far from original giant landslide. *Nature*. 450, 541-544.

497 Talling, P.J., Masson, G.D., Sumner, J.E., Malgesini, G., 2012. Subaqueous sediment density flows: Depositional  
 498 processes and deposit types. *Sedimentology*. 59, 1937-2003.

499 Taylor, B., E. Hayes, D., 1983. Origin and History of the South China Sea Basin. Washington DC American  
 500 Geophysical Union Geophysical Monograph Series. 27, 23-56.

501 Vellinga, A., J.B. Cartigny, M.J.B., Eggenhuisen, J., Hansen, W.M.E., 2017. Morphodynamics and depositional  
 502 signature of low-aggradation cyclic steps: New insights from a depth-resolved numerical model. *Sedimentology*.  
 503 65, 540-560.

504 Wang P., Li Q., 2009. The South China Sea - Paleooceanography and Sedimentology. Springer.

505 Wang, X.J., B. Liu., J. Qian., X. Zhang., Y. Guo., P. Su., J. Liang., J. Jin., Z. Luan., D. Chen., S. XiC. Li., 2018.  
 506 Geophysical evidence for gas hydrate accumulation related to methane seepage in the Taixinan Basin, South  
 507 China Sea. *Journal of Asian Earth Sciences*. 168, 27-37.

508 Wells, M. G. 2009. How Coriolis forces can limit the spatial extent of sediment deposition of a large-scale turbidity  
 509 current. *Sedimentary Geology*. 218: 1-5.

510 Wynn, R.B., Stow, D., 2002. Classification and characterisation of deep-water sediment waves. *Marine Geology -*  
 511 *MAR GEOLOGY*. 192, 7-22.

512 Xie, X., Müller, R.D., Li, S., Gong, Z., Steinberger, B., 2006. Origin of anomalous subsidence along the Northern  
 513 South China Sea margin and its relationship to dynamic topography. *Marine and Petroleum Geology*. 23, 745-  
 514 765.

515 Yin, S., Wang, L., Guo, Y., Zhong, G., 2015. Morphology, sedimentary characteristics, and origin of the Dongsha  
 516 submarine canyon in the northeastern continental slope of the South China Sea. *Science China Earth Sciences*.

517 58, 971-985.

518 Yu, H.S., Chiang, C.S., 1994. Morphology and origin of the Hongtsai submarine canyon west of the Hengchun  
519 Peninsula, Taiwan. J. Geol. Soc. China. 38, 81-92.

520 Yu, H.S., Hong, E., 2006. Shifting submarine canyons and development of a foreland basin in SW Taiwan: controls of  
521 foreland sedimentation and longitudinal sediment transport. Journal of Asian Earth Sciences. 27, 922-932.

522 Zhang, Y., Liu, Z., Zhao, Y., Colin, C., Zhang, X., Wang, M., Zhao, S., Kneller, B., 2018. Long-term in situ  
523 observations on typhoon-triggered turbidity currents in the deep sea. Geology. 46, 675-678.

524 Zhong, G., Cartigny, M.J.B., Kuang, Z., Wang, L., 2015. Cyclic steps along the South Taiwan Shoal and West Penghu  
525 submarine canyons on the northeastern continental slope of the South China Sea. Geological Society of America  
526 Bulletin. 127, 804-824.

## 527 **Notation**

528  $A_y$  asymmetry of cyclic steps, defined as  $L_{stoss}/L_{lee}$

529  $C$  volume sediment concentration

530  $C_{fb}$  coefficient of friction at the bed

531  $C_{fi}$  coefficient of friction at the interface between the flow and ambient fluid

532  $e_w$  entrainment rate of ambient water into the current

533  $g$  gravitational acceleration

534  $R$   $(\rho_{sed}-\rho_w)/\rho_w$  ( $\rho_{sed}$  and  $\rho_w$  denote the densities of the sediment and clear water, respectively)

535  $R_i$  Richardson number

536  $S$  slope of the canyon

537  $W_1$  bankfull width at trough

538	<b>W<sub>3</sub></b> bankfull width at cyclic step crest
539	<b>W<sub>1</sub>/H<sub>1</sub></b> width to depth ratio at trough
540	<b>W<sub>3</sub>/H<sub>3</sub></b> width to depth ratio at cyclic step crest
541	<b>H<sub>1</sub></b> flow depth before hydraulic jump
542	<b>H<sub>2</sub></b> flow depth post hydraulic jump
543	<b>H<sub>3</sub></b> flow depth at step crest
544	<b>α</b> stoss side slope angle
545	<b>β</b> lee side slope angle
546	<b>θ</b> slope angle of cyclic step
547	<b>L<sub>stoss</sub></b> stoss side length
548	<b>L<sub>lee</sub></b> lee side length
549	<b>L<sub>step</sub></b> length of cyclic steps (wavelength)
550	<b>H<sub>step</sub></b> height of cyclic steps (waveheight)
551	<b>V<sub>1</sub></b> flow velocity before hydraulic jump
552	<b>V<sub>2</sub></b> flow velocity after hydraulic jump
553	<b>V<sub>3</sub></b> flow velocity at cyclic step crest
554	<b>F<sub>r1</sub></b> densimetric Froude number before hydraulic jump
555	<b>F<sub>r2</sub></b> densimetric Froude number after hydraulic jump
556	<b>F<sub>r3</sub></b> densimetric Froude number at cyclic step crest
557	<b>Q<sub>1</sub></b> bankfull discharge before hydraulic jump
558	<b>Q<sub>3</sub></b> bankfull discharge at cyclic step crest
559	<b>Δ<sub>el</sub></b> energy loss of hydraulic jump

## 560 Equations

$$561 \quad 0 = \frac{SC_{fb}^{-1}}{1 + \frac{ew(1+0.5R_i)}{C_{fb}}} - \frac{1}{R_i} \quad (1)$$

$$562 \quad e_w = \frac{0.0075}{\sqrt{1+718R_i^{2.4}}} \quad (2)$$

$$563 \quad C_{fi} = e_w(1 + 0.5R_i) \quad (3)$$

$$564 \quad r = \frac{C_{fi}}{C_{fb}} \quad (4)$$

$$565 \quad V^2 = \left(\frac{1}{1+r}\right) \frac{RCgHS}{C_{fb}} \quad (5)$$

$$566 \quad Q = VWH \quad (6)$$

$$567 \quad F_r = \frac{V}{\sqrt{RCgH}} \quad (7)$$

568 Where  $e_w$  is the dimensionless coefficient of the entrainment of ambient water into turbidity currents;  $C_{fi}$  is the  
 569 coefficient of friction at the surface of the flow;  $C_{fb}$  is the coefficient of friction at the canyon bed (ranging from  
 570 0.002 to 0.005, as suggested by Konsoer et al., 2013);  $S$  denotes the slope of the canyon bed;  $R$  is the submerged  
 571 specific gravity defined as  $R = (\rho_{sed} - \rho_w) / \rho_w$ , with  $\rho_{sed}$  the density of the sediment and  $\rho_w$  the density of the clear  
 572 water;  $C$  is the volume sediment concentration (ranging from 0.2% to 0.6%, as suggested by Konsoer et al., 2013);  
 573  $g$  is gravitational acceleration ( $9.81 \text{ m/s}^2$ ); and  $H$  is the bankfull depth of the canyon.

$$574 \quad F_{r_2} = \frac{2^{1.5} F_{r_1}}{(\sqrt{1+8F_{r_1}^2} - 1)^{1.5}} \quad (8)$$

$$575 \quad H_2 = 0.5H_1(\sqrt{1+8F_{r_1}^2} - 1) \quad (9)$$

$$576 \quad V_2 = \frac{H_1 V_1}{H_2} \quad (10)$$

577 Where  $H_1$  is the flow depth of bankfull turbidity currents before hydraulic jumps,  $F_{r1}$  and  $F_{r2}$  are the Froude number  
 578 of bankfull turbidity currents before and after the hydraulic jumps, respectively.

$$579 \quad \Delta_{el} = \frac{(H_2 - H_1)^3}{4H_1H_2} \quad (11)$$

$$580 \quad L_{jump} = H_1(160 \tanh(\frac{F_{r1}}{20}) - 12) \quad (12)$$

581 Where  $\Delta_{el}$  is the loss energy of hydraulic jumps,  $H_1$  and  $H_2$  are the flow depth before and after the hydraulic jumps,

582        respectively.  $L_{\text{jump}}$  is defined as the distance between the front and downstream faces of the jump.  $F_{r1}$  is the Froude  
583        number of bankfull turbidity currents before the hydraulic jumps.  
584

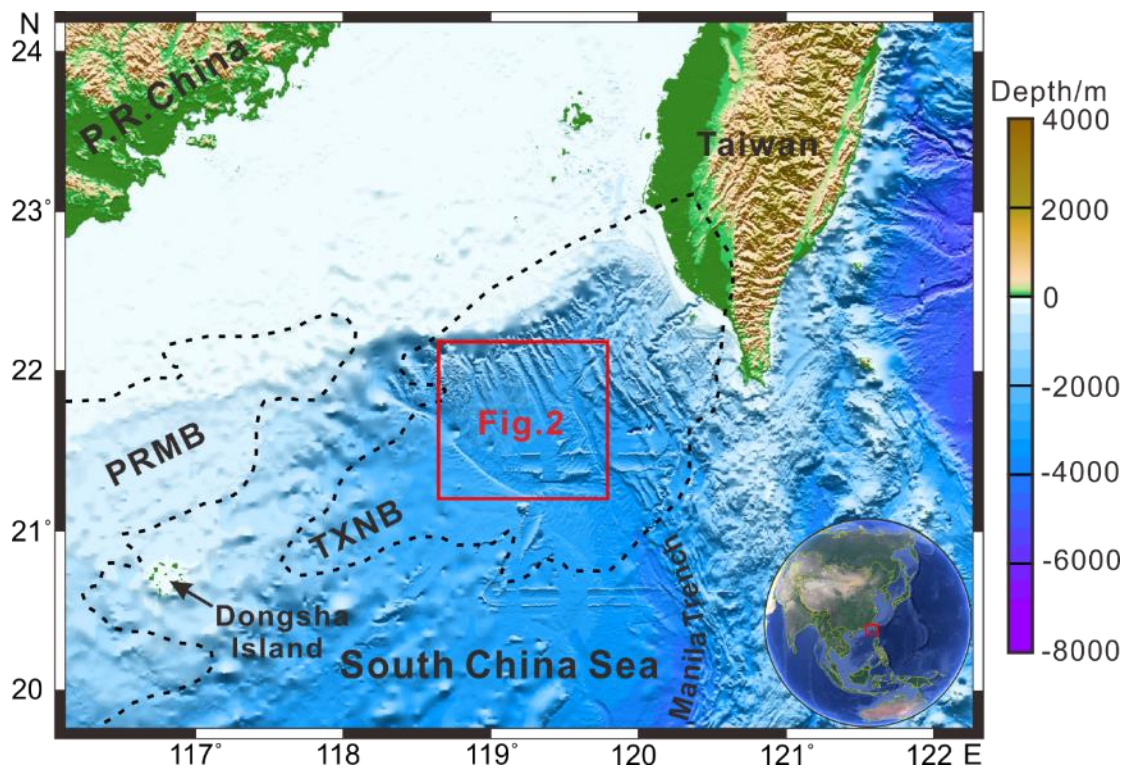
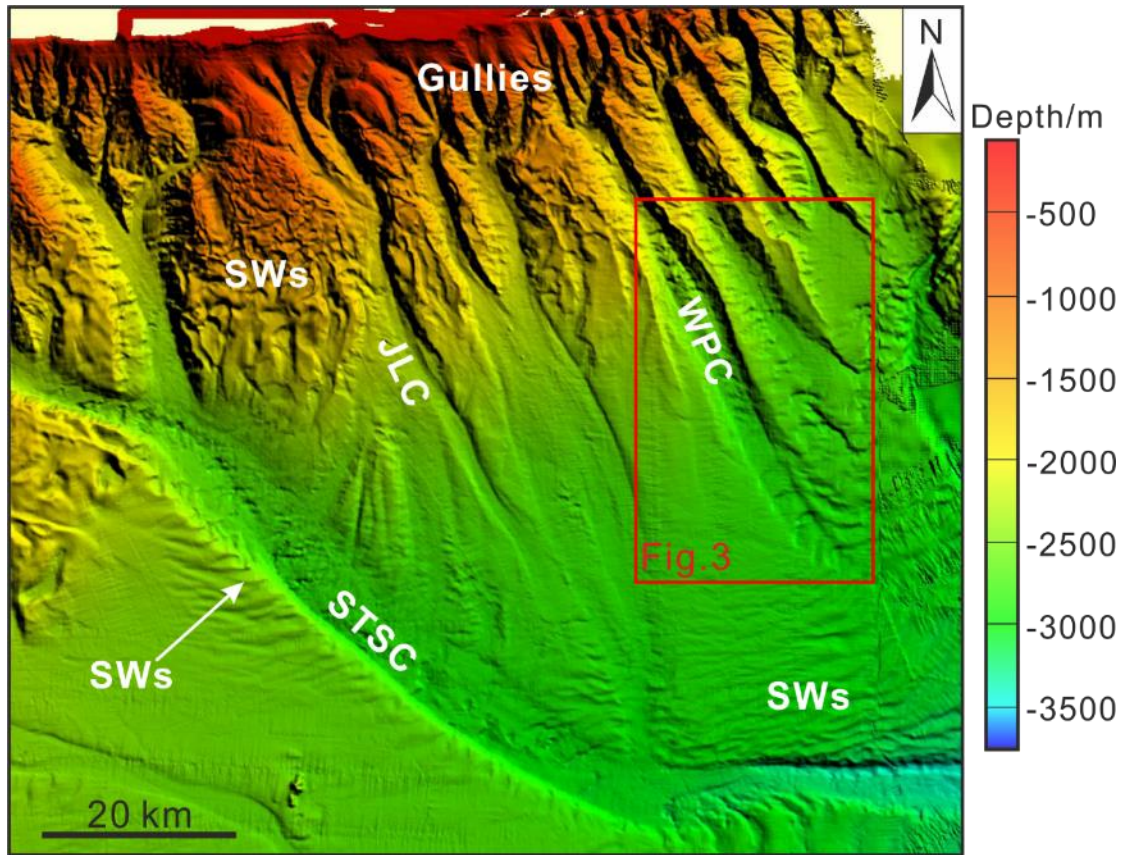


Fig. 1

586  
587 Regional map of the Taixinan Basin, northeast South China Sea, revealing the detailed location of the  
588 study area. The black dotted lines represent the boundaries of the Pearl River Mouth and Taixinan  
589 Basins. The red box indicates the location of Figure 2, which lies in the central part of Taixinan Basin.  
590 Major bathymetric features, such as the Dongsha Island and the Manila Trench, are marked in the  
591 figure. PRMB – Pearl River Mouth Basin; TXNB – Taixinan Basin.



592

593

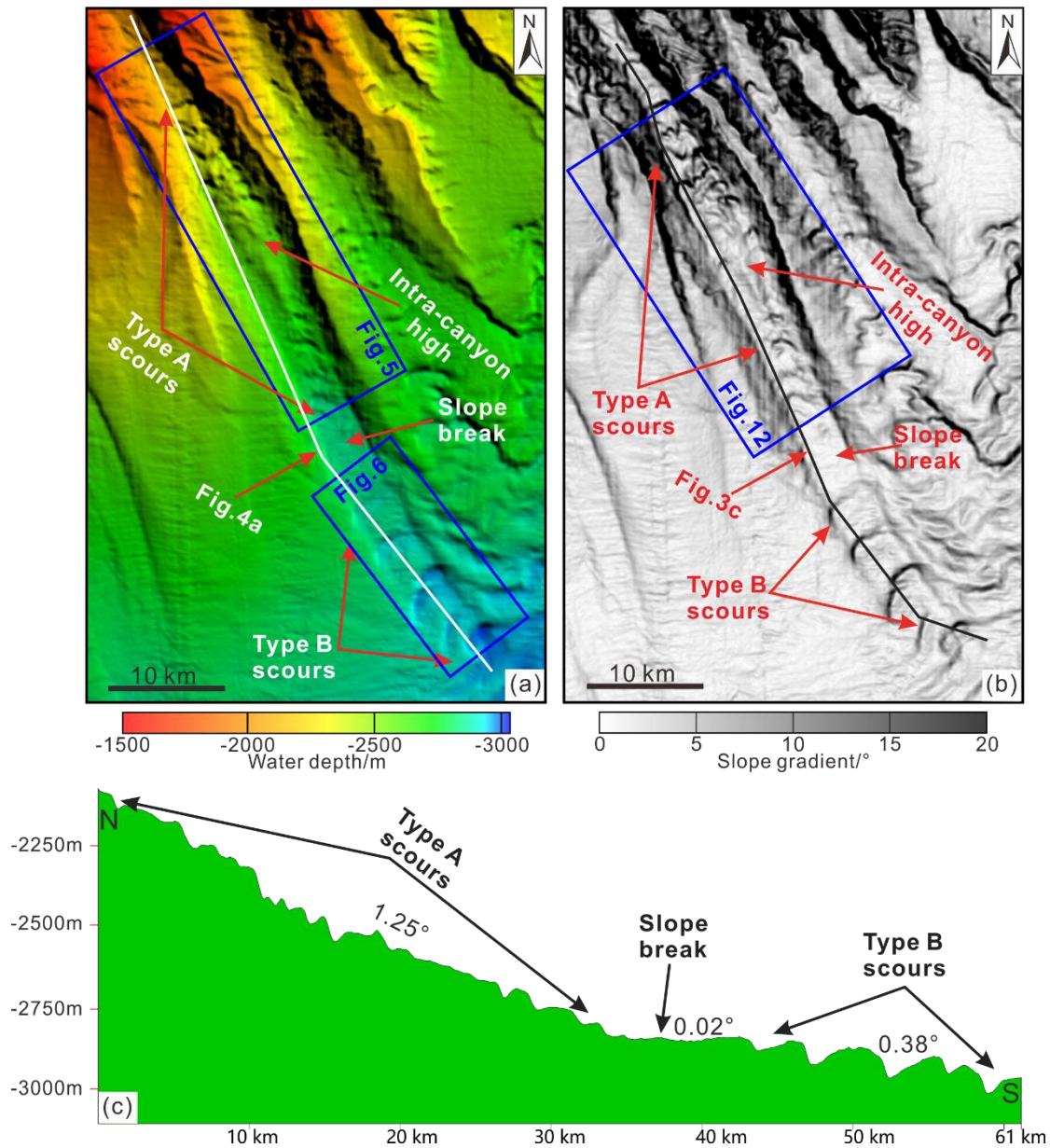
594

595

596

Fig. 2 High-resolution multibeam bathymetric map of the study area showing several submarine canyons with large gullies in their heads. The red box represents the location of Figure 3. Widespread sediment waves can be observed in the downslope region of these submarine canyons. SWs: sediment waves; STSC: South Taiwan Shoal Canyon; JLC: Jiulong Canyon; WPC: West Penghu Canyon.





597

598

599

600

601

602

603

604

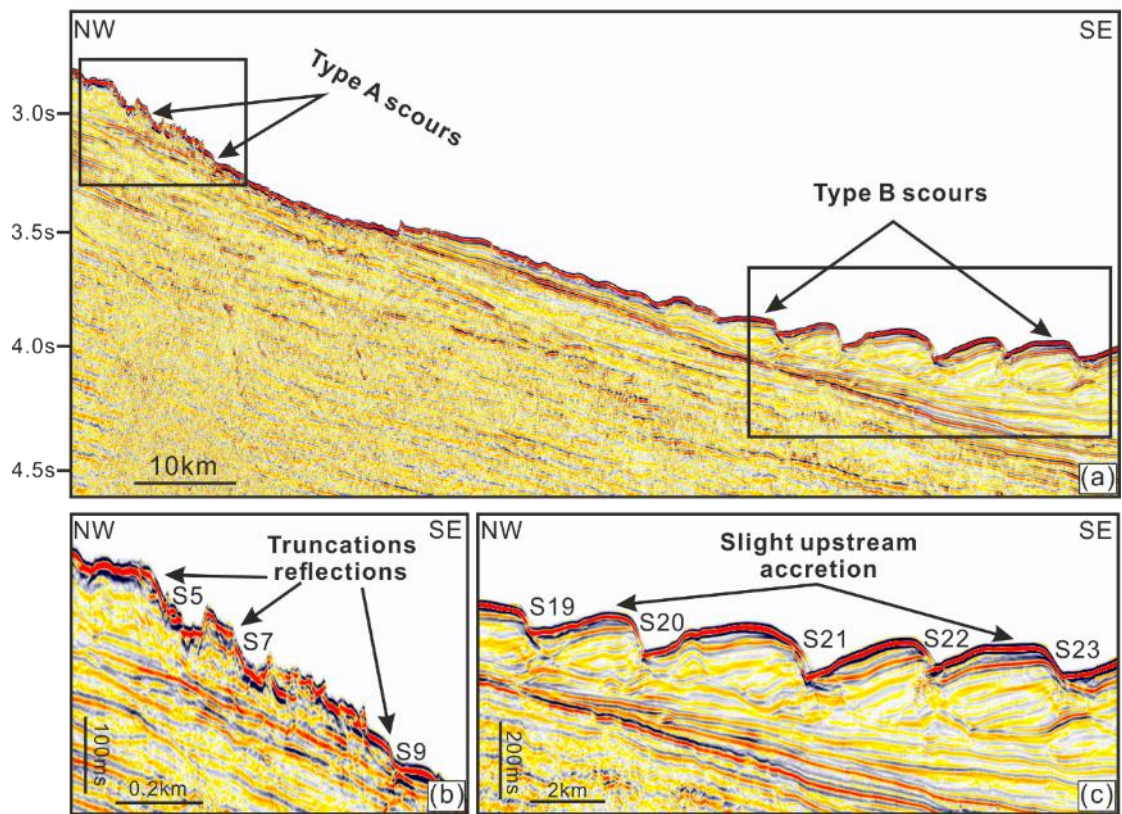
605

606

607

Fig. 3 (a) Multibeam bathymetric map illustrating the morphology and distribution of scours along the thalweg of the West Penghu Canyon (WPC) at a water depth of 1500 m to 3000 m. The blue boxes indicate the areas shown in Figure 5 (Type A scours) and 6 (Type B scours). The white line shows the location of the seismic profile in Figure 4a. A slope break can be identified at a water depth of ~2850 m. (b) Slope gradient map illustrating the morphology of Type A and B scours along the thalweg of the West Penghu Canyon. The blue box indicates the area shown in Figure 12, and an intra-canyon high is marked in this area. The black line indicates the cross-section profile shown in Figure 3c. (c) Bathymetric profile along the thalweg of the West Penghu Canyon showing two different type of scours (Types A and B) separated by a slope break. Note that Type B scours are much larger than Type A scours.





608

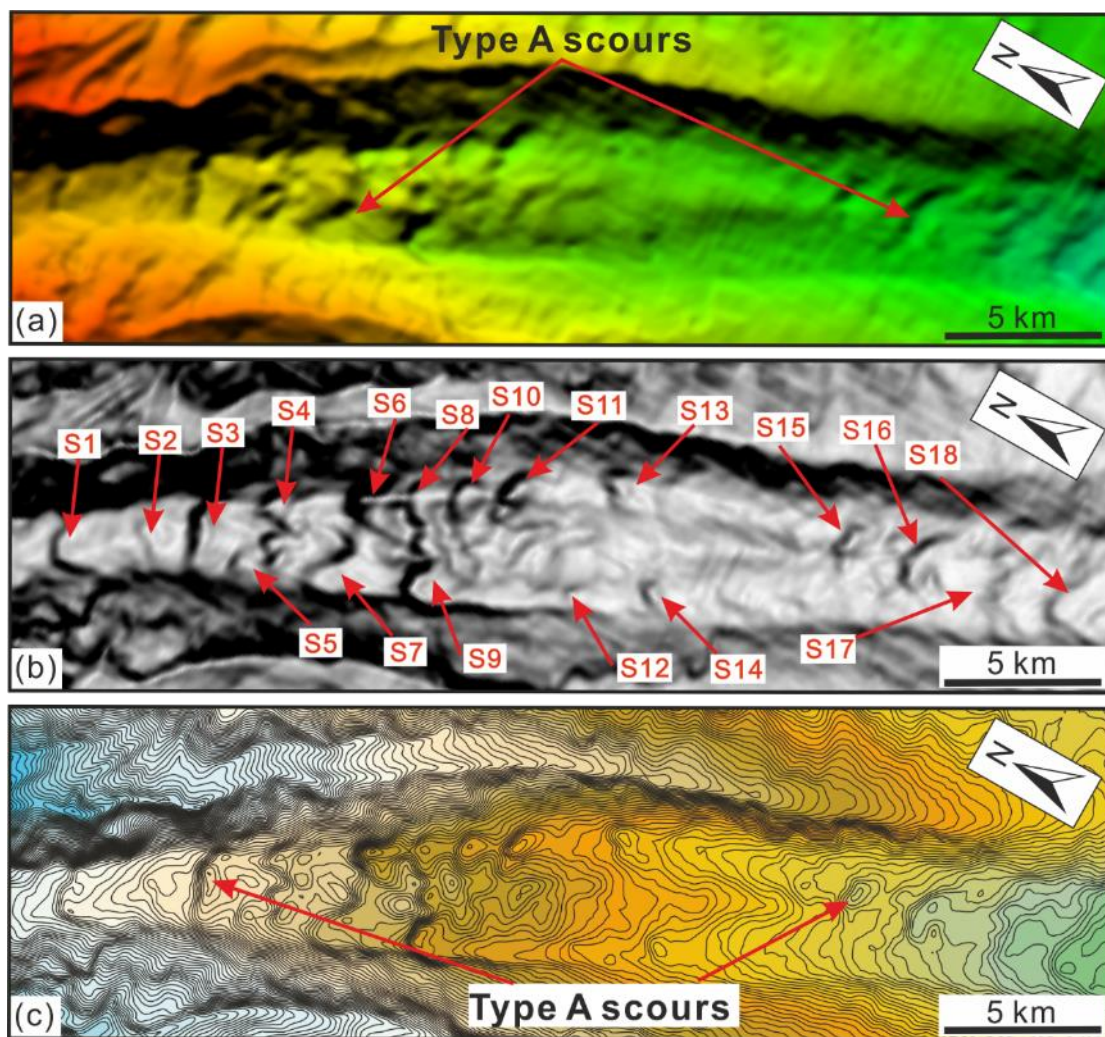
609

610

611

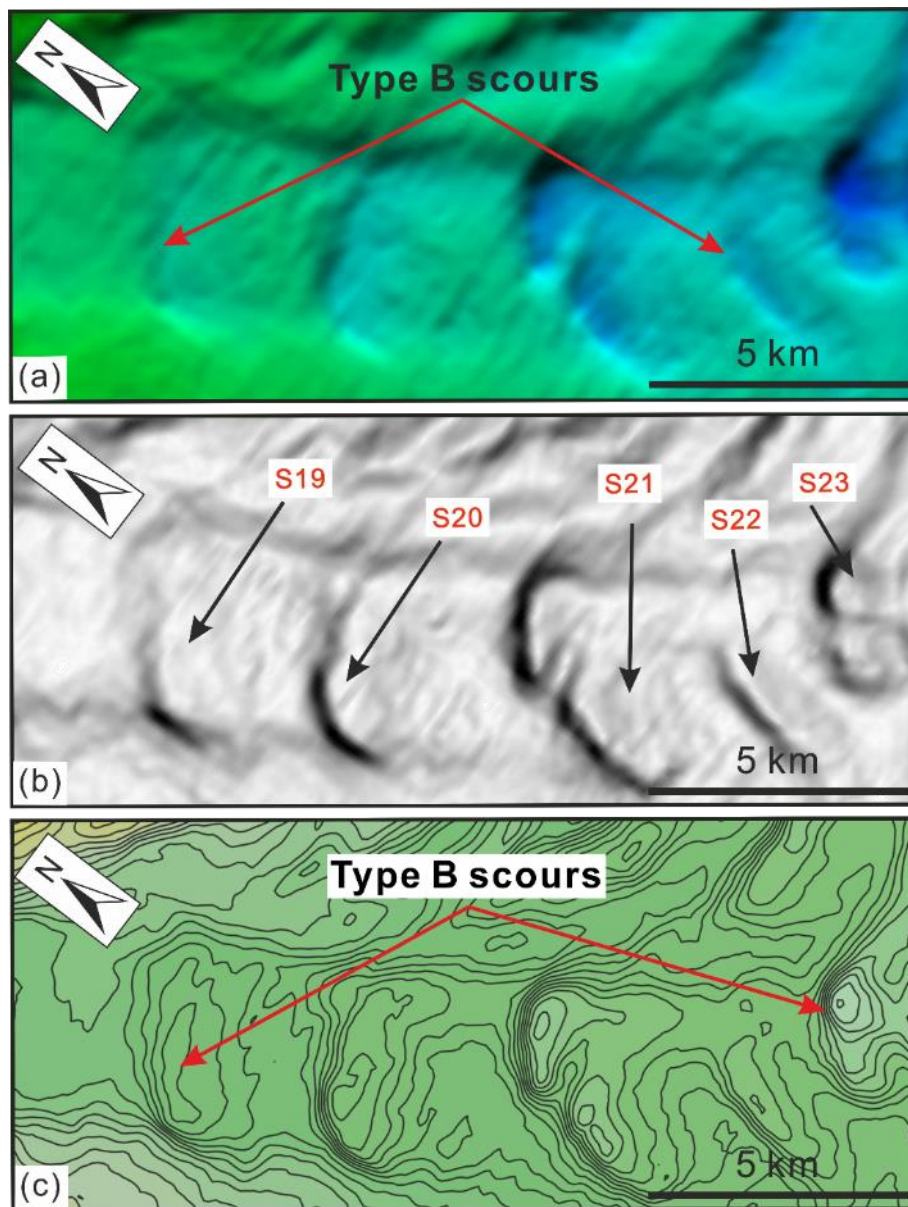
612

Fig. 4 (a) 2D multichannel seismic profile of the seismic line in Figure 3a. The black boxes indicate the Type A scours and Type B scours shown in Figures 4b and 4c, respectively. (b) Truncated reflections are observed in the stoss sides of Type A scours (S5, S7, S9). (c) Slight upstream accretions are observed in the lee sides of the Type B scours.



613  
 614 Fig. 5 (a) Multibeam bathymetric map showing the detailed morphology of Type A scours in the  
 615 upslope region of the West Penghu Canyon. (b) Eighteen (18) Type A scours (S1 to S18) are marked  
 616 on the slope gradient map from northwest to southeast. (c) The contour map illustrates the distribution  
 617 of several enclosed depressions, which are interpreted as Type A scours.





618  
 619 Fig. 6 (a) Multibeam bathymetric map showing the detailed morphology of Type B scours in the  
 620 deeper, lower-slope region of the West Penghu Canyon. (b) Five (5) Type B scours (S19 to S23) are  
 621 marked on the slope gradient map from northwest to southeast. (c) The contour map illustrates the  
 622 distribution of several enclosed depressions, interpreted as Type B scours.

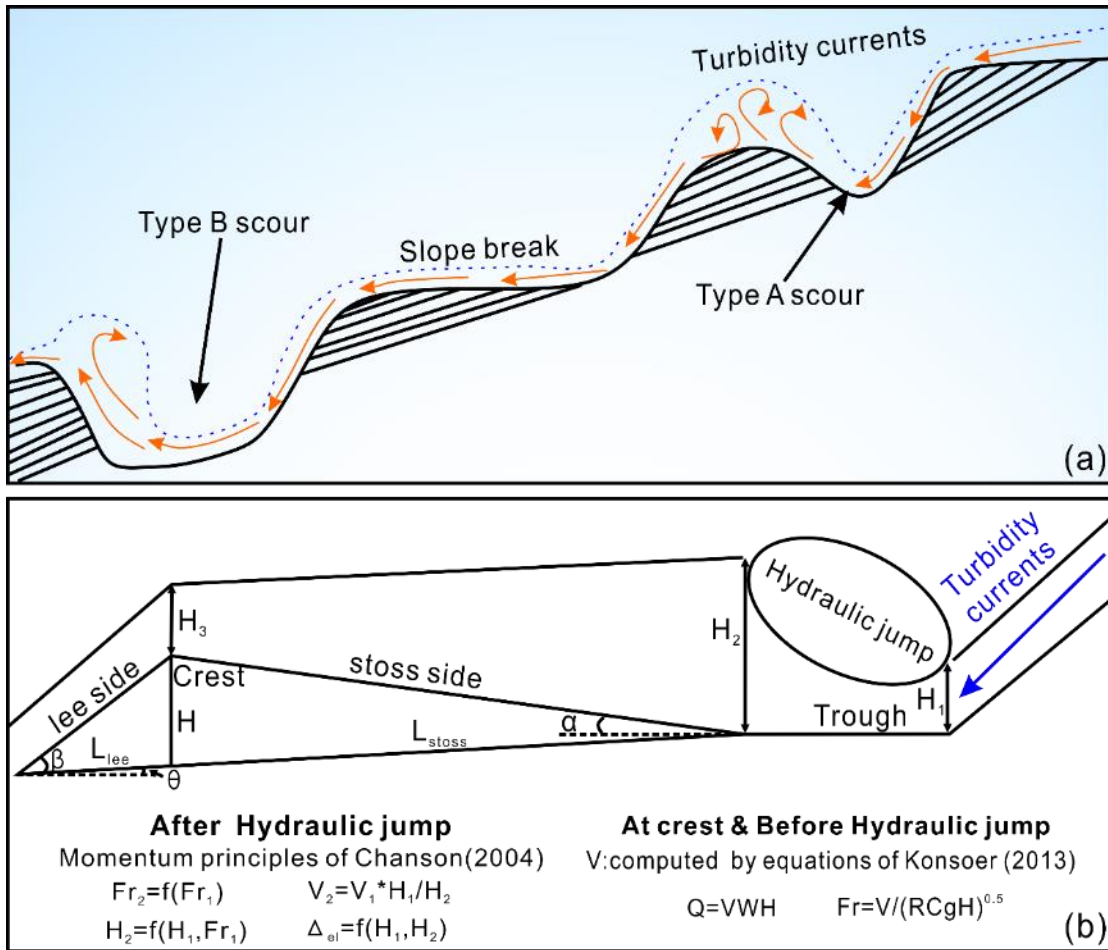
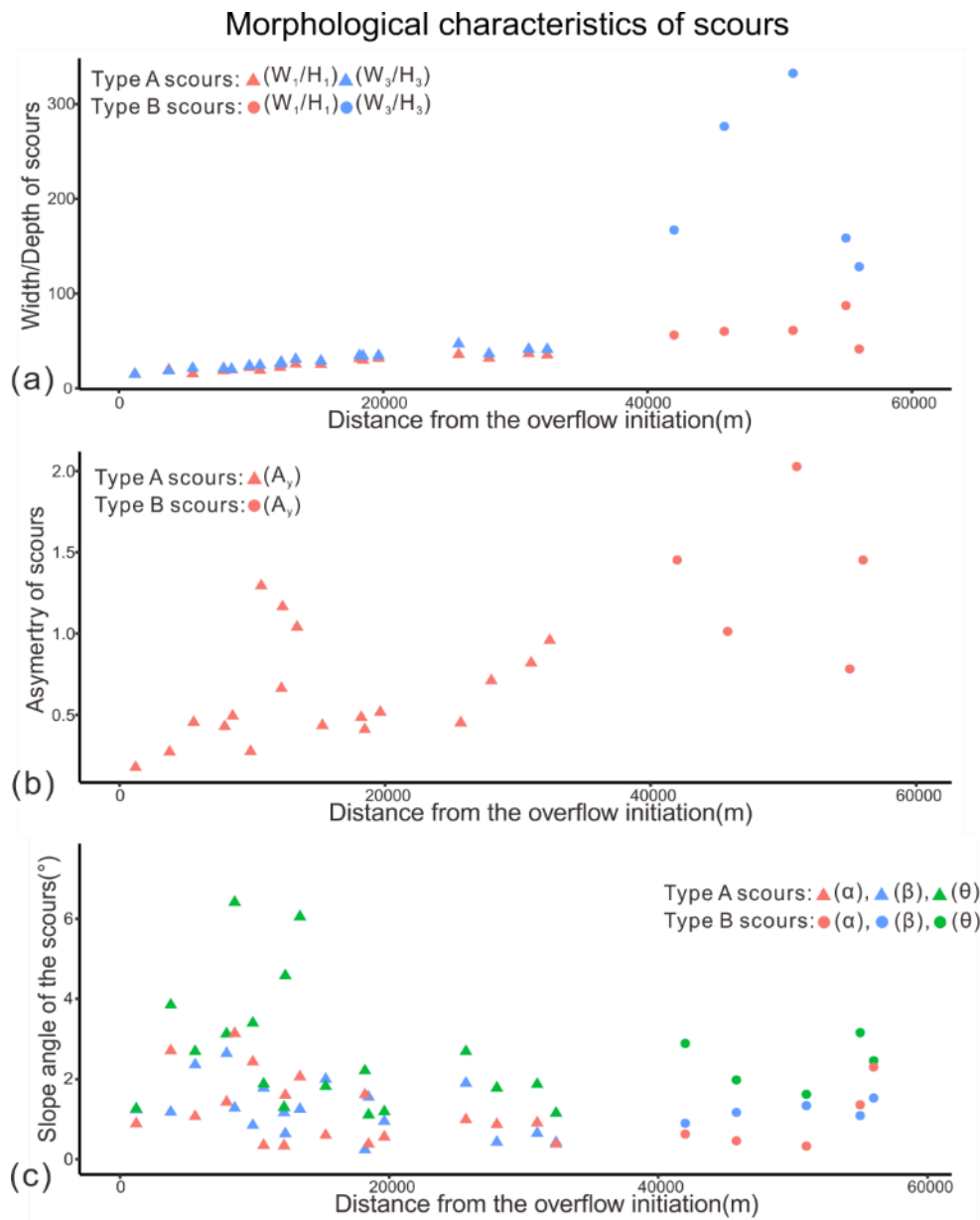


Fig. 7 (a) Schematic diagram depicting the transition from Type A to Type B scours in the region where a slope break is located. The blue dotted line represents the flow depth, while the orange arrows indicate the internal flow structures of overriding turbidity currents (flow is from right to left). (b) Schematic illustration of a single scour showing its morphological parameters (modified by Li and Gong, 2018), and the three locations where the bankfull hydraulics are calculated by using the formulas for turbidity current conditions in this work: (1) at the base of the lee slope just before the hydraulic jump, (2) at the crest of the scour, and (3) at the base of the stoss slope just after the hydraulic jump.



632

633

634

635

636

637

638

Fig. 8 Morphological characteristics of scours in the West Penghu Canyon. (a) Distance from the overflow initiation vs.  $W/H$ . The ratio  $W_1/H_1$  is marked in red, while the ratio  $W_3/H_3$  is indicated in blue. (b) Distance from the overflow initiation vs.  $A_y$ . (c) Distance from the overflow initiation vs. slope angle. Slope gradients of the stoss side ( $\alpha$ ), the lee side ( $\beta$ ) and the scour ( $\theta$ ) are marked in red, blue and green, respectively. Note that the triangles represent Type A scours and the circles indicate Type B scours for the three figures above.

### Hydraulic characteristics of scours

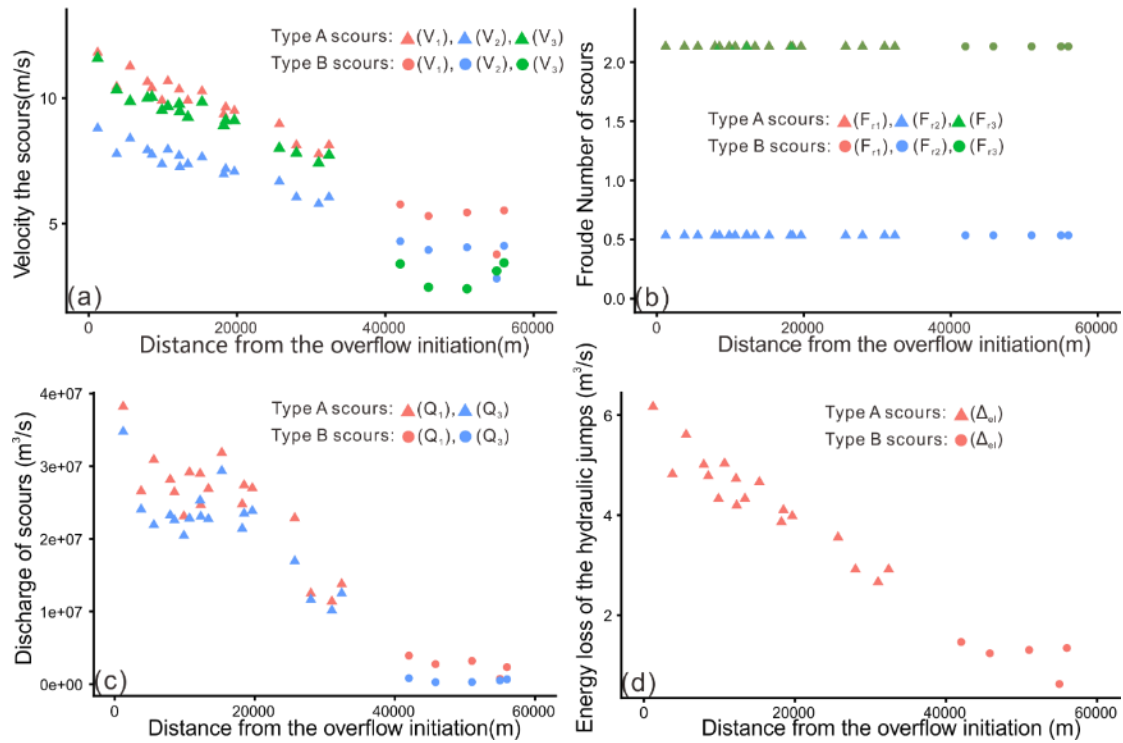
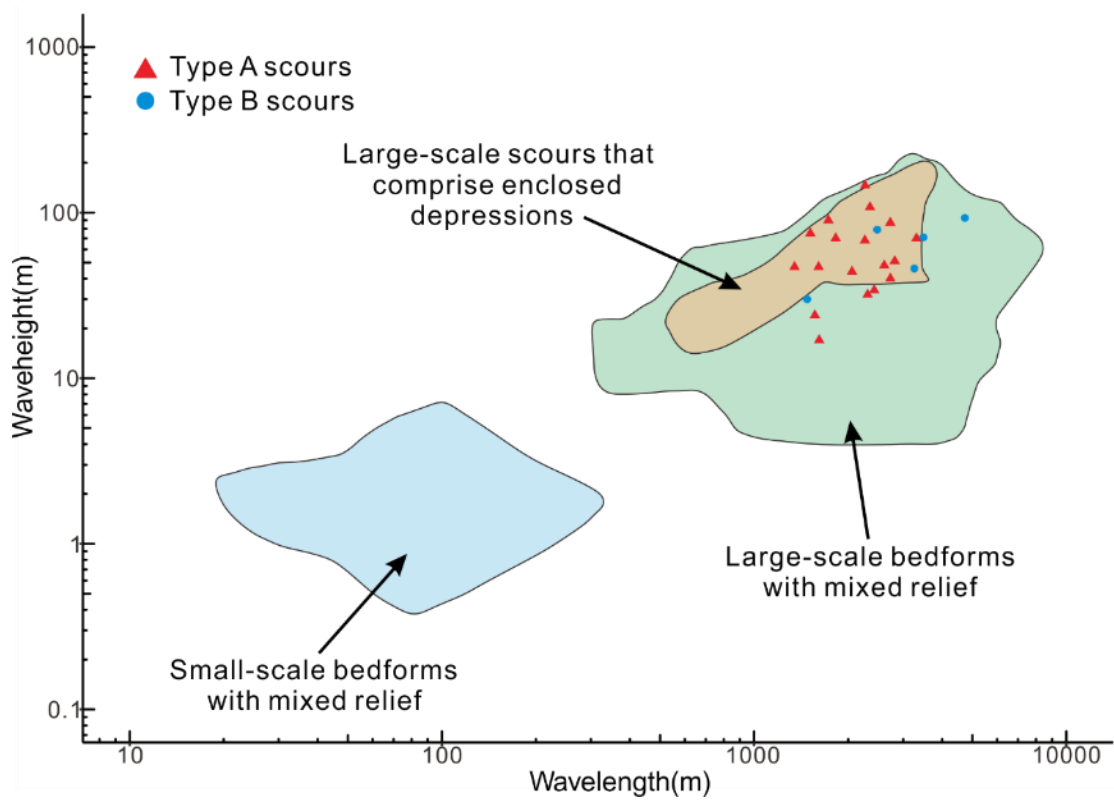


Fig. 9 Hydraulic characteristics of scours in the West Penghu Canyon. (a) Distance from the overflow initiation vs.  $V$ , the red represents  $V_1$  (velocity at the trough), the blue represents  $V_2$  (velocity after the hydraulic jumps) and the green symbolizes  $V_3$  (velocity at the crest). (b) Distance from the overflow initiation vs.  $Fr$ . Red, blue and green colors denote  $Fr_1$  (Froude number at the trough),  $Fr_2$  (Froude number after the hydraulic jump), and  $Fr_3$  (Froude number at the crest), respectively. (c) Distance from the overflow initiation vs. discharge. In red is  $Q_1$  (discharge at the trough) and in blue is  $Q_3$  (discharge at the crest). (d) Distance from the overflow initiation vs.  $\Delta_{el}$ . The triangles represent Type A scours and the circles indicate Type B scours.



648

649 Fig. 10 Logarithmic plots of aspect ratios (wavelength vs. wave height) for twenty-three (23) scours  
 650 along the thalweg of the West Penghu Canyon, compared to those described in Symons et al. (2016).

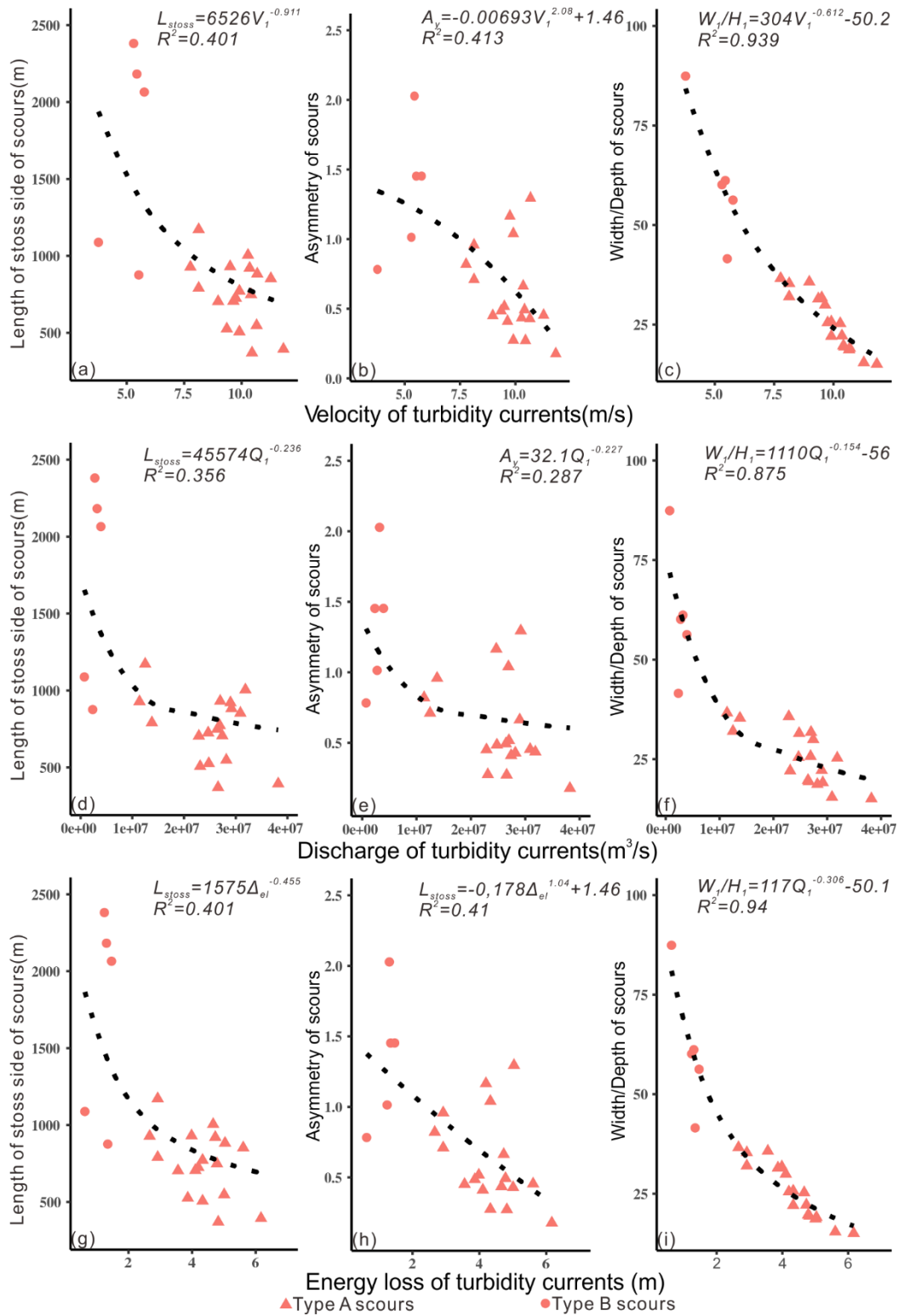
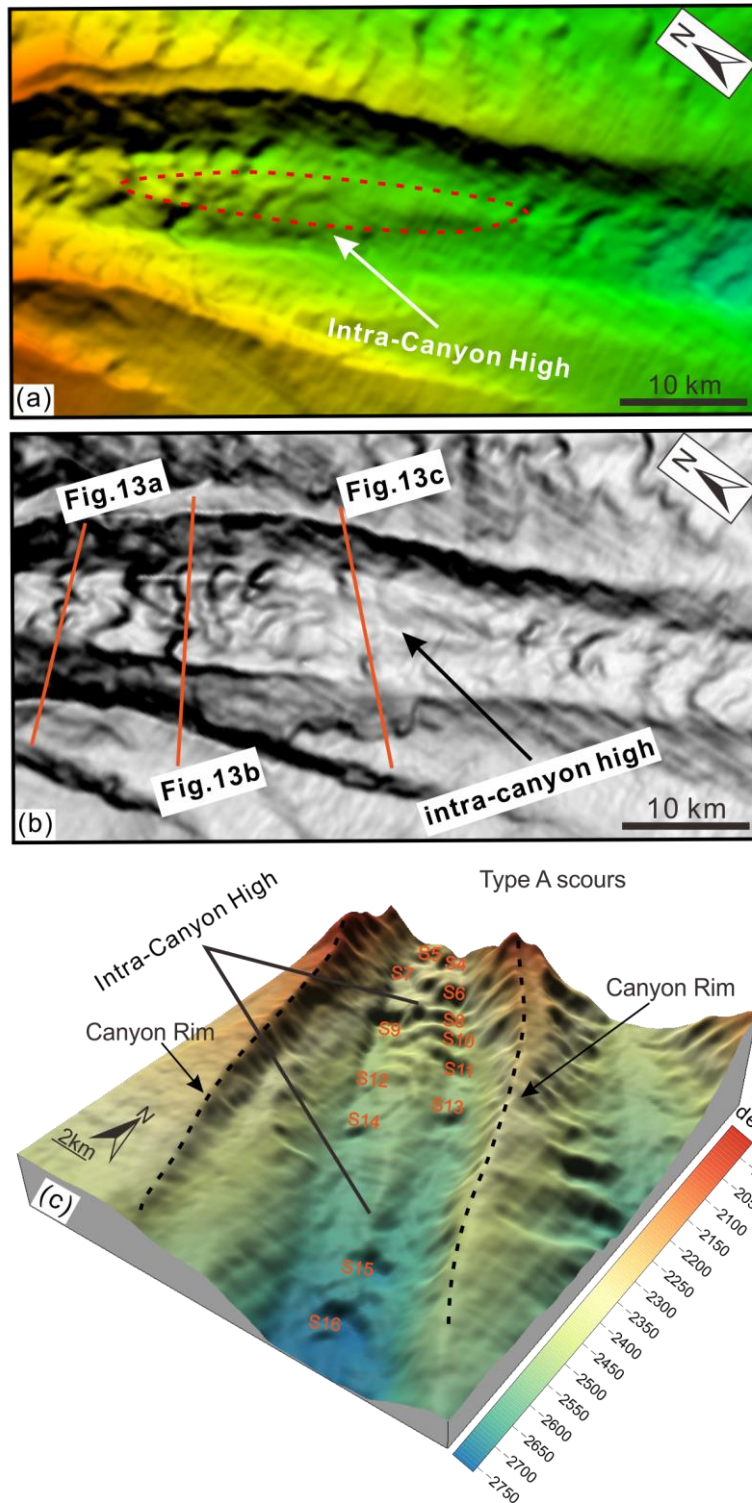


Fig.11 Morphological characteristics and properties of turbidity currents in the West Penghu Canyon, showing relationships of cyclic step morphological characteristics and turbidity current properties. Triangles and circles denote net Type A and B scours, respectively.





656

657 Fig. 12 (a) Multibeam bathymetric map showing the detailed morphology of the intra-canyon high in  
 658 the upper reach of the West Penghu Canyon. The red dotted line indicates the location of the intra-  
 659 canyon high at a water depth of 2000 m to 2750 m. (b) The intra-canyon high can also be distinguished  
 660 on the slope gradient map, while the orange solid lines represent the bathymetric profiles shown in  
 661 Figures 13a, b and c. (c) 3D perspective view of the upper reach of the West Penghu Canyon showing  
 662 two trains of Type A scours which are separated by the intra-canyon high.

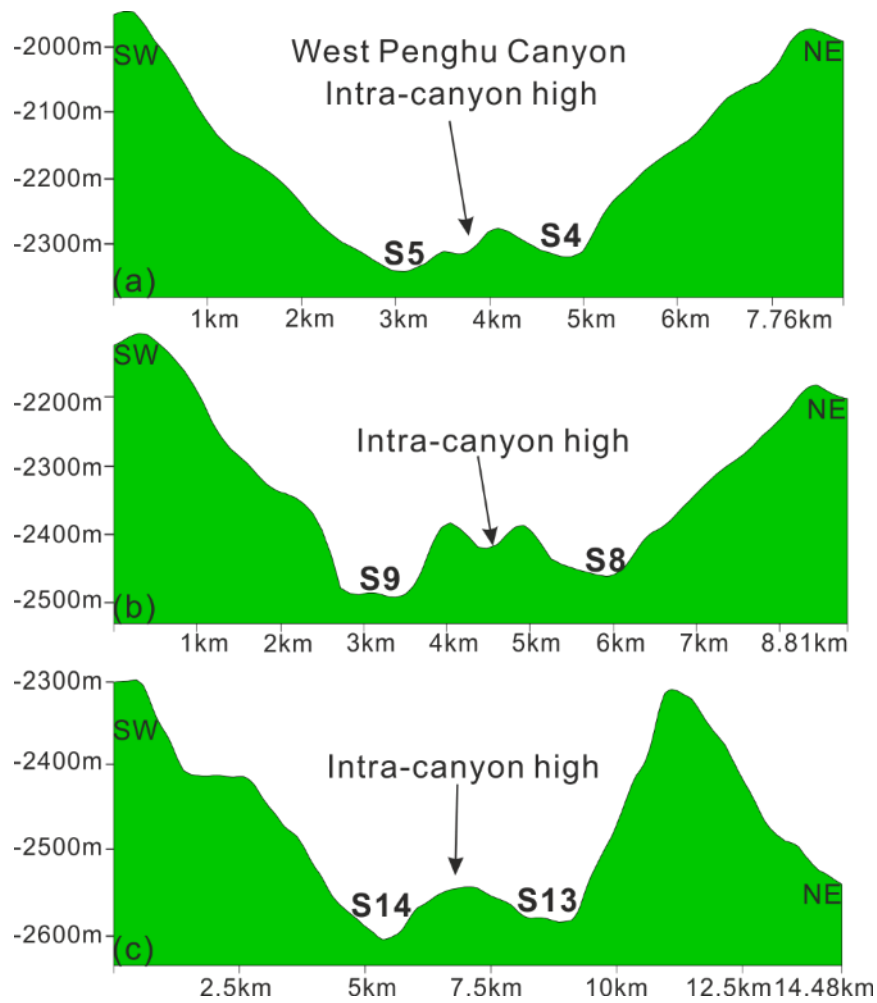
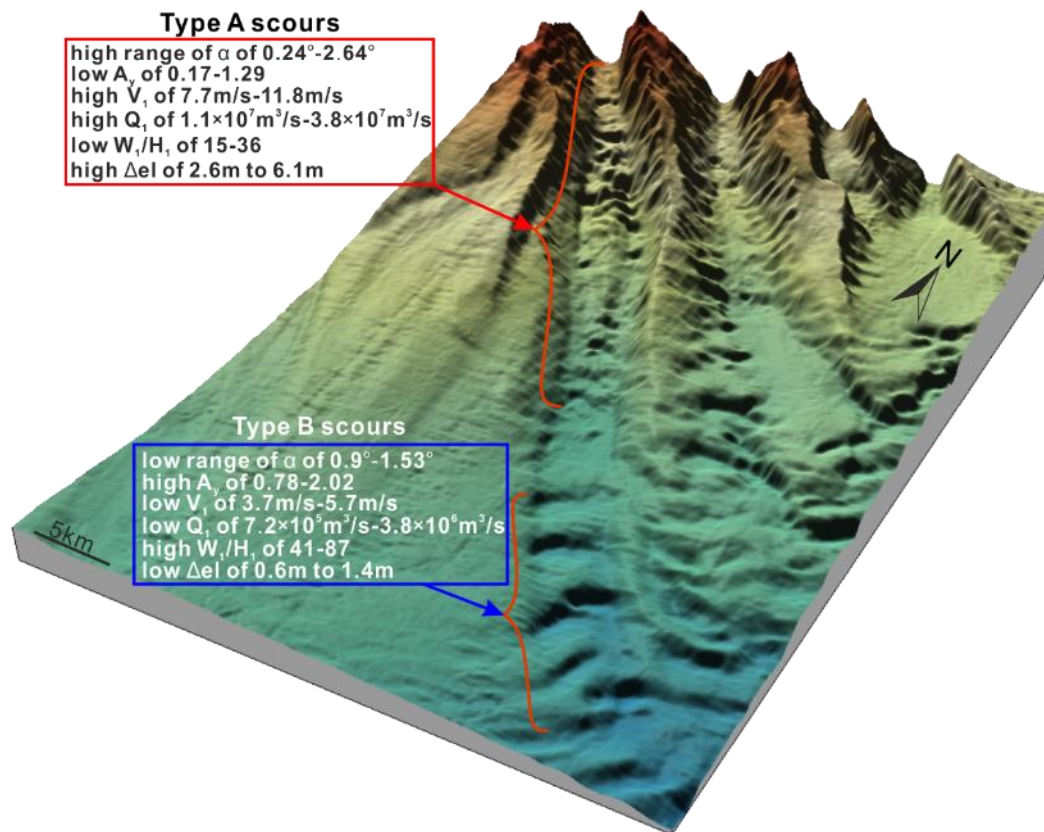


Fig.13 Bathymetric profiles crossing (a) scours 4 and 5, (b) scours 8 and 9, and (c) scours 13 and 14. The profiles show that scours to the southwest of the intra-canyon high are more deeply incised than their counterparts to the northeast.



667

668 Fig. 14 3D view of the West Penghu Canyon showing Type A scours in its upper reach and Type B  
 669 scours in its lower reach. Differences in morphological parameters ( $A_y$ ,  $\alpha$ , and  $W_1/H_1$ ) and the  
 670 estimated properties of turbidity currents ( $V_1$ ,  $Q_1$ , and  $\Delta_{el}$ ) are shown in the figure for Type A and B  
 671 scours.